PHYSICAL REVIEW D **83,** 052001 (2011)

Dalitz plot analysis of $D_s^+ \to K^+K^-\pi^+$

P. del Amo Sanchez,[1] J. P. Lees,[1] V. Poireau,[1] E. Prencipe,[1] V. Tisserand,[1] J. Garra Tico,[2] E. Grauges,[2] M. Martinelli,[3a,3b] D. A. Milanes,[3a,3b] A. Palano,[3a,3b] M. Pappagallo,[3a,3b] G. Eigen,[4] B. Stugu,[4] L. Sun,[4] D. N. Brown,[5] L. T. Kerth,[5] Yu. G. Kolomensky,[5] G. Lynch,[5] I. L. Osipenkov,[5] H. Koch,[6] T. Schroeder,[6] D. J. Asgeirsson,[7] C. Hearty,[7] T. S. Mattison,[7] J. A. McKenna,[7] A. Khan,[8] V. E. Blinov,[9] A. R. Buzykaev,[9] V. P. Druzhinin,[9] V. B. Golubev,[9] E. A. Kravchenko,[9] A. P. Onuchin,[9] S. I. Serednyakov,[9] Yu. I. Skovpen,[9] E. P. Solodov,[9] K. Yu. Todyshev,[9] A. N. Yushkov,[9] M. Bondioli,[10] S. Curry,[10] D. Kirkby,[10] A. J. Lankford,[10] M. Mandelkern,[10] E. C. Martin,[10] D. P. Stoker,[10] H. Atmacan,[11] J. W. Gary,[11] F. Liu,[11] O. Long,[11] G. M. Vitug,[11] C. Campagnari,[12] T. M. Hong,[12] D. Kovalskyi,[12] J. D. Richman,[12] C. West,[12] A. M. Eisner,[13] C. A. Heusch,[13] J. Kroseberg,[13] W. S. Lockman,[13] A. J. Martinez,[13] T. Schalk,[13] B. A. Schumm,[13] A. Seiden,[13] L. O. Winstrom,[13] C. H. Cheng,[14] D. A. Doll,[14] B. Echenard,[14] D. G. Hitlin,[14] P. Ongmongkolkul,[14] F. C. Porter,[14] A. Y. Rakitin,[14] R. Andreassen,[15] M. S. Dubrovin,[15] G. Mancinelli,[15] B. T. Meadows,[15] M. D. Sokoloff,[15] P. C. Bloom,[16] W. T. Ford,[16] A. Gaz,[16] M. Nagel,[16] U. Nauenberg,[16] J. G. Smith,[16] S. R. Wagner,[16] R. Ayad,[17,*] W. H. Toki,[17] H. Jasper,[18] T. M. Karbach,[18] A. Petzold,[18] B. Spaan,[18] M. J. Kobel,[19] K. R. Schubert,[19] R. Schwierz,[19] D. Bernard,[20] M. Verderi,[20] P. J. Clark,[21] S. Playfer,[21] J. E. Watson,[21] M. Andreotti,[22a,22b] D. Bettoni,[22a] C. Bozzi,[22a] R. Calabrese,[22a,22b] A. Cecchi,[22a,22b] G. Cibinetto,[22a,22b] E. Fioravanti,[22a,22b] P. Franchini,[22a,22b] I. Garzia,[22a,22b] E. Luppi,[22a,22b] M. Munerato,[22a,22b] M. Negrini,[22a,22b] A. Petrella,[22a,22b] L. Piemontese,[22a] R. Baldini-Ferroli,[23] A. Calcaterra,[23] R. de Sangro,[23] G. Finocchiaro,[23] M. Nicolaci,[23] S. Pacetti,[23] P. Patteri,[23] I. M. Peruzzi,[23,†] M. Piccolo,[23] M. Rama,[23] A. Zallo,[23] R. Contri,[24a,24b] E. Guido,[24a,24b] M. Lo Vetere,[24a,24b] M. R. Monge,[24a,24b] S. Passaggio,[24a] C. Patrignani,[24a,24b] E. Robutti,[24a] S. Tosi,[24a,24b] B. Bhuyan,[25] V. Prasad,[25] C. L. Lee,[26] M. Morii,[26] A. J. Edwards,[27] A. Adametz,[28] J. Marks,[28] U. Uwer,[28] F. U. Bernlochner,[29] M. Ebert,[29] H. M. Lacker,[29] T. Lueck,[29] A. Volk,[29] P. D. Dauncey,[30] M. Tibbetts,[30] P. K. Behera,[31] U. Mallik,[31] C. Chen,[32] J. Cochran,[32] H. B. Crawley,[32] L. Dong,[32] W. T. Meyer,[32] S. Prell,[32] E. I. Rosenberg,[32] A. E. Rubin,[32] A. V. Gritsan,[33] Z. J. Guo,[33] N. Arnaud,[34] M. Davier,[34] D. Derkach,[34] J. Firmino da Costa,[34] G. Grosdidier,[34] F. Le Diberder,[34] A. M. Lutz,[34] B. Malaescu,[34] A. Perez,[34] P. Roudeau,[34] M. H. Schune,[34] J. Serrano,[34] V. Sordini,[34,‡] A. Stocchi,[34] L. Wang,[34] G. Wormser,[34] D. J. Lange,[35] D. M. Wright,[35] I. Bingham,[36] C. A. Chavez,[36] J. P. Coleman,[36] J. R. Fry,[36] E. Gabathuler,[36] R. Gamet,[36] D. E. Hutchcroft,[36] D. J. Payne,[36] C. Touramanis,[36] A. J. Bevan,[37] F. Di Lodovico,[37] R. Sacco,[37] M. Sigamani,[37] G. Cowan,[38] S. Paramesvaran,[38] A. C. Wren,[38] D. N. Brown,[39] C. L. Davis,[39] A. G. Denig,[40] M. Fritsch,[40] W. Gradl,[40] A. Hafner,[40] K. E. Alwyn,[41] D. Bailey,[41] R. J. Barlow,[41] G. Jackson,[41] G. D. Lafferty,[41] J. Anderson,[42] R. Cenci,[42] A. Jawahery,[42] D. A. Roberts,[42] G. Simi,[42] J. M. Tuggle,[42] C. Dallapiccola,[43] E. Salvati,[43] R. Cowan,[44] D. Dujmic,[44] G. Sciolla,[44] M. Zhao,[44] D. Lindemann,[45] P. M. Patel,[45] S. H. Robertson,[45] M. Schram,[45] P. Biassoni,[46a,46b] A. Lazzaro,[46a,46b] V. Lombardo,[46a] F. Palombo,[46a,46b] S. Stracka,[46a,46b] L. Cremaldi,[47] R. Godang,[47,§] R. Kroeger,[47] P. Sonnek,[47] D. J. Summers,[47] X. Nguyen,[48] M. Simard,[48] P. Taras,[48] G. De Nardo,[49a,49b] D. Monorchio,[49a,49b] G. Onorato,[49a,49b] C. Sciacca,[49a,49b] G. Raven,[50] H. L. Snoek,[50] C. P. Jessop,[51] K. J. Knoepfel,[51] J. M. LoSecco,[51] W. F. Wang,[51] L. A. Corwin,[52] K. Honscheid,[52] R. Kass,[52] J. P. Morris,[52] N. L. Blount,[53] J. Brau,[53] R. Frey,[53] O. Igonkina,[53] J. A. Kolb,[53] R. Rahmat,[53] N. B. Sinev,[53] D. Strom,[53] J. Strube,[53] E. Torrence,[53] G. Castelli,[54a,54b] E. Feltresi,[54a,54b] N. Gagliardi,[54a,54b] M. Margoni,[54a,54b] M. Morandin,[54a] M. Posocco,[54a] M. Rotondo,[54a] F. Simonetto,[54a,54b] R. Stroili,[54a,54b] E. Ben-Haim,[55] G. R. Bonneaud,[55] H. Briand,[55] G. Calderini,[55] J. Chauveau,[55] O. Hamon,[55] Ph. Leruste,[55] G. Marchiori,[55] J. Ocariz,[55] J. Prendki,[55] S. Sitt,[55] M. Biasini,[56a,56b] E. Manoni,[56a,56b] A. Rossi,[56a,56b] C. Angelini,[57a,57b] G. Batignani,[57a,57b] S. Bettarini,[57a,57b] M. Carpinelli,[57a,57b,∥] G. Casarosa,[57a,57b] A. Cervelli,[57a,57b] F. Forti,[57a,57b] M. A. Giorgi,[57a,57b] A. Lusiani,[57a,57c] N. Neri,[57a,57b] E. Paoloni,[57a,57b] G. Rizzo,[57a,57b] J. J. Walsh,[57a] D. Lopes Pegna,[58] C. Lu,[58] J. Olsen,[58] A. J. S. Smith,[58] A. V. Telnov,[58] F. Anulli,[59a] E. Baracchini,[59a,59b] G. Cavoto,[59a] R. Faccini,[59a,59b] F. Ferrarotto,[59a] F. Ferroni,[59a,59b] M. Gaspero,[59a,59b] L. Li Gioi,[59a] M. A. Mazzoni,[59a] G. Piredda,[59a] F. Renga,[59a,59b] T. Hartmann,[60] T. Leddig,[60] H. Schröder,[60] R. Waldi,[60] T. Adye,[61] B. Franek,[61] E. O. Olaiya,[61] F. F. Wilson,[61] S. Emery,[62] G. Hamel de Monchenault,[62] G. Vasseur,[62] Ch. Yèche,[62] M. Zito,[62] M. T. Allen,[63] D. Aston,[63] D. J. Bard,[63] R. Bartoldus,[63] J. F. Benitez,[63] C. Cartaro,[63] M. R. Convery,[63] J. Dorfan,[63] G. P. Dubois-Felsmann,[63] W. Dunwoodie,[63] R. C. Field,[63] M. Franco Sevilla,[63] B. G. Fulsom,[63] A. M. Gabareen,[63] M. T. Graham,[63] P. Grenier,[63] C. Hast,[63] W. R. Innes,[63] M. H. Kelsey,[63] H. Kim,[63] P. Kim,[63] M. L. Kocian,[63] D. W. G. S. Leith,[63] S. Li,[63] B. Lindquist,[63] S. Luitz,[63] V. Luth,[63] H. L. Lynch,[63] D. B. MacFarlane,[63] H. Marsiske,[63] D. R. Muller,[63] H. Neal,[63] S. Nelson,[63] C. P. O'Grady,[63] I. Ofte,[63] M. Perl,[63] T. Pulliam,[63] B. N. Ratcliff,[63] A. Roodman,[63] A. A. Salnikov,[63] V. Santoro,[63] R. H. Schindler,[63] J. Schwiening,[63] A. Snyder,[63] D. Su,[63] M. K. Sullivan,[63] S. Sun,[63] K. Suzuki,[63] J. M. Thompson,[63] J. Va'vra,[63]

A. P. Wagner,[63] M. Weaver,[63] W. J. Wisniewski,[63] M. Wittgen,[63] D. H. Wright,[63] H. W. Wulsin,[63] A. K. Yarritu,[63] C. C. Young,[63] V. Ziegler,[63] X. R. Chen,[64] W. Park,[64] M. V. Purohit,[64] R. M. White,[64] J. R. Wilson,[64] A. Randle-Conde,[65] S. J. Sekula,[65] M. Bellis,[66] P. R. Burchat,[66] T. S. Miyashita,[66] S. Ahmed,[67] M. S. Alam,[67] J. A. Ernst,[67] B. Pan,[67] M. A. Saeed,[67] S. B. Zain,[67] N. Guttman,[68] A. Soffer,[68] P. Lund,[69] S. M. Spanier,[69] R. Eckmann,[70] J. L. Ritchie,[70] A. M. Ruland,[70] C. J. Schilling,[70] R. F. Schwitters,[70] B. C. Wray,[70] J. M. Izen,[71] X. C. Lou,[71] F. Bianchi,[72a,72b] D. Gamba,[72a,72b] M. Pelliccioni,[72a,72b] M. Bomben,[73a,73b] L. Lanceri,[73a,73b] L. Vitale,[73a,73b] N. Lopez-March,[74] F. Martinez-Vidal,[74] A. Oyanguren,[74] J. Albert,[75] Sw. Banerjee,[75] H. H. F. Choi,[75] K. Hamano,[75] G. J. King,[75] R. Kowalewski,[75] M. J. Lewczuk,[75] C. Lindsay,[75] I. M. Nugent,[75] J. M. Roney,[75] R. J. Sobie,[75] T. J. Gershon,[76] P. F. Harrison,[76] T. E. Latham,[76] M. R. Pennington,[76,¶] E. M. T. Puccio,[76] H. R. Band,[77] S. Dasu,[77] K. T. Flood,[77] Y. Pan,[77] R. Prepost,[77] C. O. Vuosalo,[77] and S. L. Wu[77]

(*BABAR* Collaboration)

[1]*Laboratoire d'Annecy-le-Vieux de Physique des Particules (LAPP), Université de Savoie, CNRS/IN2P3, F-74941 Annecy-Le-Vieux, France*
[2]*Universitat de Barcelona, Facultat de Fisica, Departament ECM, E-08028 Barcelona, Spain*
[3a]*INFN Sezione di Bari, I-70126 Bari, Italy;*
[3b]*Dipartimento di Fisica, Università di Bari, I-70126 Bari, Italy*
[4]*University of Bergen, Institute of Physics, N-5007 Bergen, Norway*
[5]*Lawrence Berkeley National Laboratory and University of California, Berkeley, California 94720, USA*
[6]*Ruhr Universität Bochum, Institut für Experimentalphysik 1, D-44780 Bochum, Germany*
[7]*University of British Columbia, Vancouver, British Columbia, Canada V6T 1Z1*
[8]*Brunel University, Uxbridge, Middlesex UB8 3PH, United Kingdom*
[9]*Budker Institute of Nuclear Physics, Novosibirsk 630090, Russia*
[10]*University of California at Irvine, Irvine, California 92697, USA*
[11]*University of California at Riverside, Riverside, California 92521, USA*
[12]*University of California at Santa Barbara, Santa Barbara, California 93106, USA*
[13]*University of California at Santa Cruz, Institute for Particle Physics, Santa Cruz, California 95064, USA*
[14]*California Institute of Technology, Pasadena, California 91125, USA*
[15]*University of Cincinnati, Cincinnati, Ohio 45221, USA*
[16]*University of Colorado, Boulder, Colorado 80309, USA*
[17]*Colorado State University, Fort Collins, Colorado 80523, USA*
[18]*Technische Universität Dortmund, Fakultät Physik, D-44221 Dortmund, Germany*
[19]*Technische Universität Dresden, Institut für Kern- und Teilchenphysik, D-01062 Dresden, Germany*
[20]*Laboratoire Leprince-Ringuet, CNRS/IN2P3, Ecole Polytechnique, F-91128 Palaiseau, France*
[21]*University of Edinburgh, Edinburgh EH9 3JZ, United Kingdom*
[22a]*INFN Sezione di Ferrara, I-44100 Ferrara, Italy;*
[22b]*Dipartimento di Fisica, Università di Ferrara, I-44100 Ferrara, Italy*
[23]*INFN Laboratori Nazionali di Frascati, I-00044 Frascati, Italy*
[24a]*INFN Sezione di Genova, I-16146 Genova, Italy;*
[24b]*Dipartimento di Fisica, Università di Genova, I-16146 Genova, Italy*
[25]*Indian Institute of Technology Guwahati, Guwahati, Assam, 781 039, India*
[26]*Harvard University, Cambridge, Massachusetts 02138, USA*
[27]*Harvey Mudd College, Claremont, California 91711*
[28]*Universität Heidelberg, Physikalisches Institut, Philosophenweg 12, D-69120 Heidelberg, Germany*
[29]*Humboldt-Universität zu Berlin, Institut für Physik, Newtonstr. 15, D-12489 Berlin, Germany*
[30]*Imperial College London, London, SW7 2AZ, United Kingdom*
[31]*University of Iowa, Iowa City, Iowa 52242, USA*
[32]*Iowa State University, Ames, Iowa 50011-3160, USA*
[33]*Johns Hopkins University, Baltimore, Maryland 21218, USA*
[34]*Laboratoire de l'Accélérateur Linéaire, IN2P3/CNRS et Université Paris-Sud 11, Centre Scientifique d'Orsay, B. P. 34, F-91898 Orsay Cedex, France*
[35]*Lawrence Livermore National Laboratory, Livermore, California 94550, USA*
[36]*University of Liverpool, Liverpool L69 7ZE, United Kingdom*
[37]*Queen Mary, University of London, London, E1 4NS, United Kingdom*
[38]*University of London, Royal Holloway and Bedford New College, Egham, Surrey TW20 0EX, United Kingdom*
[39]*University of Louisville, Louisville, Kentucky 40292, USA*

[40]Johannes Gutenberg-Universität Mainz, Institut für Kernphysik, D-55099 Mainz, Germany
[41]University of Manchester, Manchester M13 9PL, United Kingdom
[42]University of Maryland, College Park, Maryland 20742, USA
[43]University of Massachusetts, Amherst, Massachusetts 01003, USA
[44]Massachusetts Institute of Technology, Laboratory for Nuclear Science, Cambridge, Massachusetts 02139, USA
[45]McGill University, Montréal, Québec, Canada H3A 2T8
[46a]INFN Sezione di Milano, I-20133 Milano, Italy;
[46b]Dipartimento di Fisica, Università di Milano, I-20133 Milano, Italy
[47]University of Mississippi, University, Mississippi 38677, USA
[48]Université de Montréal, Physique des Particules, Montréal, Québec, Canada H3C 3J7
[49a]INFN Sezione di Napoli, I-80126 Napoli, Italy;
[49b]Dipartimento di Scienze Fisiche, Università di Napoli Federico II, I-80126 Napoli, Italy
[50]NIKHEF, National Institute for Nuclear Physics and High Energy Physics, NL-1009 DB Amsterdam, The Netherlands
[51]University of Notre Dame, Notre Dame, Indiana 46556, USA
[52]Ohio State University, Columbus, Ohio 43210, USA
[53]University of Oregon, Eugene, Oregon 97403, USA
[54a]INFN Sezione di Padova, I-35131 Padova, Italy;
[54b]Dipartimento di Fisica, Università di Padova, I-35131 Padova, Italy
[55]Laboratoire de Physique Nucléaire et de Hautes Energies, IN2P3/CNRS, Université Pierre et Marie Curie-Paris6, Université Denis Diderot-Paris7, F-75252 Paris, France
[56a]INFN Sezione di Perugia, I-06100 Perugia, Italy;
[56b]Dipartimento di Fisica, Università di Perugia, I-06100 Perugia, Italy
[57a]INFN Sezione di Pisa, I-56127 Pisa, Italy;
[57b]Dipartimento di Fisica, Università di Pisa, I-56127 Pisa, Italy;
[57c]Scuola Normale Superiore di Pisa, I-56127 Pisa, Italy
[58]Princeton University, Princeton, New Jersey 08544, USA
[59a]INFN Sezione di Roma, I-00185 Roma, Italy;
[59b]Dipartimento di Fisica, Università di Roma La Sapienza, I-00185 Roma, Italy
[60]Universität Rostock, D-18051 Rostock, Germany
[61]Rutherford Appleton Laboratory, Chilton, Didcot, Oxon, OX11 0QX, United Kingdom
[62]CEA, Irfu, SPP, Centre de Saclay, F-91191 Gif-sur-Yvette, France
[63]SLAC National Accelerator Laboratory, Stanford, California 94309 USA
[64]University of South Carolina, Columbia, South Carolina 29208, USA
[65]Southern Methodist University, Dallas, Texas 75275, USA
[66]Stanford University, Stanford, California 94305-4060, USA
[67]State University of New York, Albany, New York 12222, USA
[68]Tel Aviv University, School of Physics and Astronomy, Tel Aviv, 69978, Israel
[69]University of Tennessee, Knoxville, Tennessee 37996, USA
[70]University of Texas at Austin, Austin, Texas 78712, USA
[71]University of Texas at Dallas, Richardson, Texas 75083, USA
[72a]INFN Sezione di Torino, I-10125 Torino, Italy;
[72b]Dipartimento di Fisica Sperimentale, Università di Torino, I-10125 Torino, Italy
[73a]INFN Sezione di Trieste, I-34127 Trieste, Italy;
[73b]Dipartimento di Fisica, Università di Trieste, I-34127 Trieste, Italy
[74]IFIC, Universitat de Valencia-CSIC, E-46071 Valencia, Spain
[75]University of Victoria, Victoria, British Columbia, Canada V8W 3P6
[76]Department of Physics, University of Warwick, Coventry CV4 7AL, United Kingdom
[77]University of Wisconsin, Madison, Wisconsin 53706, USA

(Received 18 November 2010; published 3 March 2011)

We perform a Dalitz plot analysis of about 100 000 D_s^+ decays to $K^+K^-\pi^+$ and measure the complex amplitudes of the intermediate resonances which contribute to this decay mode. We also measure the relative branching fractions of $D_s^+ \to K^+K^+\pi^-$ and $D_s^+ \to K^+K^+K^-$. For this analysis we use a

*Now at Temple University, Philadelphia, PA 19122, USA
†Also with Università di Perugia, Dipartimento di Fisica, Perugia, Italy.
‡Also with Università di Roma La Sapienza, I-00185 Roma, Italy.
§Now at University of South AL, Mobile, AL 36688, USA.
‖Also with Università di Sassari, Sassari, Italy.
¶Also with Institute for Particle Physics Phenomenology, Durham University, Durham DH1 3LE, UK.

384 fb^{-1} data sample, recorded by the *BABAR* detector at the PEP-II asymmetric-energy e^+e^- collider running at center-of-mass energies near 10.58 GeV.

DOI: 10.1103/PhysRevD.83.052001 PACS numbers: 13.25.Ft, 11.80.Et, 14.40.Be, 14.40.Lb

I. INTRODUCTION

Scalar mesons are still a puzzle in light meson spectroscopy. New claims for the existence of broad states close to threshold such as $\kappa(800)$ [1] and $f_0(600)$ [2], have reopened discussion about the composition of the ground state $J^{PC} = 0^{++}$ nonet, and about the possibility that states such as the $a_0(980)$ or $f_0(980)$ may be 4-quark states, due to their proximity to the $K\bar{K}$ threshold [3]. This hypothesis can be tested only through accurate measurements of the branching fractions and the couplings to different final states. It is therefore important to have precise information on the structure of the $\pi\pi$ and $K\bar{K}$ $\mathcal{S}$ waves. In this context, D_s^+ mesons can shed light on the structure of the scalar amplitude coupled to $s\bar{s}$. The $\pi\pi$ $\mathcal{S}$ wave has been already extracted from *BABAR* data in a Dalitz plot analysis of $D_s^+ \to \pi^+\pi^-\pi^+$ [4]. The understanding of the $K\bar{K}$ $\mathcal{S}$ wave is also of great importance for the precise measurement of CP violation in B_s oscillations using $B_s \to J/\psi\phi$ [5,6].

This paper focuses on the study of D_s^+ meson decay to $K^+K^-\pi^+$ [7]. Dalitz plot analyses of this decay mode have been performed by the E687 and CLEO Collaborations using 700 events [8], and 14 400 events [9] respectively. The present analysis is performed using about 100 000 events.

The decay $D_s^+ \to \phi\pi^+$ is frequently used in particle physics as the reference mode for D_s^+ decay. Previous measurements of this decay mode did not, however, account for the presence of the $K\bar{K}$ $\mathcal{S}$ wave underneath the ϕ peak. Therefore, as part of the present analysis, we obtain a precise measurement of the branching fraction $\mathcal{B}(D_s^+ \to \phi\pi^+)$ relative to $\mathcal{B}(D_s^+ \to K^+K^-\pi^+)$.

Singly Cabibbo-suppressed (SCS) and doubly Cabibbo-suppressed (DCS) decays play an important role in studies of charmed hadron dynamics. The naive expectations for the rates of SCS and DCS decays are of the order of $\tan^2\theta_C$ and $\tan^4\theta_C$, respectively, where θ_C is the Cabibbo mixing angle. These rates correspond to about 5.3% and 0.28% relative to their Cabibbo-favored (CF) counterpart. Because of the limited statistics in past experiments, branching fraction measurements of DCS decays have been affected by large statistical uncertainties [10]. A precise measurement of $\frac{\mathcal{B}(D_s^+ \to K^+K^+\pi^-)}{\mathcal{B}(D_s^+ \to K^+K^-\pi^+)}$ has been recently performed by the Belle experiment [11].

In this paper we study the D_s^+ decay

$$D_s^+ \to K^+K^-\pi^+ \tag{1}$$

and perform a detailed Dalitz plot analysis. We then measure the branching ratios of the SCS decay

$$D_s^+ \to K^+K^-K^+ \tag{2}$$

and the DCS decay

$$D_s^+ \to K^+K^+\pi^- \tag{3}$$

relative to the CF channel (1). The paper is organized as follows. Section II briefly describes the *BABAR* detector, while Sec. III gives details of event reconstruction. Section IV is devoted to the evaluation of the selection efficiency. Section V describes a partial-wave analysis of the K^+K^- system, the evaluation of the $D_s^+ \to \phi\pi^+$ branching fraction, and the $K\bar{K}$ $\mathcal{S}$-wave parametrization. Section VI deals with the description of the Dalitz plot analysis method and background description. Results from the Dalitz plot analysis of $D_s^+ \to K^+K^-\pi^+$ are given in Sec. VII. The measurements of the D_s^+ SCS and DCS branching fractions are described in Sec. VIII, while Sec. IX summarizes the results.

II. THE *BABAR* DETECTOR AND DATASET

The data sample used in this analysis corresponds to an integrated luminosity of 384 fb^{-1} recorded with the *BABAR* detector at the SLAC PEP-II collider, operated at center-of-mass energies near the $\Upsilon(4S)$ resonance. The *BABAR* detector is described in detail elsewhere [12]. The following is a brief summary of the components important to this analysis. Charged particle tracks are detected, and their momenta measured, by a combination of a cylindrical drift chamber and a silicon vertex tracker, both operating within a 1.5 T solenoidal magnetic field. Photon energies are measured with a CsI(Tl) electromagnetic calorimeter. Information from a ring-imaging Cherenkov detector, and specific energy-loss measurements in the silicon vertex tracker and cylindrical drift chamber are used to identify charged kaon and pion candidates.

III. EVENT SELECTION AND $D_s^+ \to K^+K^-\pi^+$ RECONSTRUCTION

Events corresponding to the three-body $D_s^+ \to K^+K^-\pi^+$ decay are reconstructed from the data sample having at least three reconstructed charged tracks with net charge ± 1. We require that the invariant mass of the $K^+K^-\pi^+$ system lie within the mass interval [1.9–2.05] GeV/c^2. Particle identification is applied to the three tracks, and the presence of two kaons is required. The efficiency that a kaon is identified is 90% while the rate that a kaon is misidentified as a pion is 2%. The three tracks are required to originate from a common vertex, and the χ^2 fit probability (P_1) must be greater than 0.1%.

We also perform a separate kinematic fit in which the D_s^+ mass is constrained to its known value [10]. This latter fit will be used only in the Dalitz plot analysis.

In order to help in the discrimination of signal from background, an additional fit is performed, constraining the three tracks to originate from the e^+e^- luminous region (beam spot). The χ^2 probability of this fit, labeled as P_2, is expected to be large for most of the background events, when all tracks originate from the luminous region, and small for the D_s^+ signal, due to the measurable flight distance of the latter.

The decay

$$D_s^*(2112)^+ \to D_s^+\gamma \tag{4}$$

is used to select a subset of event candidates in order to reduce combinatorial background. The photon is required to have released an energy of at least 100 MeV into the electromagnetic calorimeter. We define the variable

$$\Delta m = m(K^+K^-\pi^+\gamma) - m(K^+K^-\pi^+) \tag{5}$$

and require it to be within $\pm 2\sigma_{D_s^{*+}}$ with respect to $\Delta m_{D_s^{*+}}$ where $\Delta m_{D_s^{*+}} = 144.94 \pm 0.03_{\rm stat}$ MeV$/c^2$ and $\sigma_{D_s^{*+}} = 5.53 \pm 0.04_{\rm stat}$ MeV$/c^2$ are obtained from a Gaussian fit of the Δm distribution.

Each D_s^+ candidate is characterized by three variables: the center-of-mass momentum p^* in the e^+e^- rest frame, the difference in probability $P_1 - P_2$, and the signed decay distance $d_{xy} = \frac{\mathbf{d}\cdot\mathbf{p}_{xy}}{|\mathbf{p}_{xy}|}$ where $\mathbf{d}$ is the vector joining the beam spot to the D_s^+ decay vertex and $\mathbf{p}_{xy}$ is the projection of the D_s^+ momentum on the xy plane. These three variables are used to discriminate signal from background events: in fact signal events are expected to be characterized by larger values of p^* [13], due to the jetlike shape of the $e^+e^- \to c\bar{c}$ events, and larger values of d_{xy} and $P_1 - P_2$, due to the measurable flight distance of the D_s^+ meson.

The distributions of these three variables for signal and background events are determined from data and are shown in Fig. 1. The background distributions are estimated from events in the D_s^+ mass-sidebands, while those for the signal region are estimated from the D_s^+ signal region with sideband subtraction. The normalized probability distribution functions are then combined in a likelihood-ratio test. A selection is performed on this variable such that signal to background ratio is maximized. Lower sideband, signal, and upper sideband regions are defined between [1.911–1.934] GeV$/c^2$, [1.957–1.980] GeV$/c^2$, and [2.003–2.026] GeV$/c^2$, respectively, corresponding to $(-10\sigma, -6\sigma)$, $(-2\sigma, 2\sigma)$, and $(6\sigma, 10\sigma)$ regions, where σ is estimated from the fit of a Gaussian function to the D_s^+ lines shape.

We have examined a number of possible background sources. A small peak due to the decay $D^{*+} \to \pi^+ D^0$ where $D^0 \to K^+K^-$ is observed. A Gaussian fit to this K^+K^- spectrum gives $\sigma_{D^0\to K^+K^-} = 5.4$ MeV$/c^2$. For events within $3.5\sigma_{D^0\to K^+K^-}$ of the D^0 mass, we plot the mass difference $\Delta m(K^+K^-\pi^+) = m(K^+K^-\pi^+) - m(K^+K^-)$ and observe a clean D^{*+} signal. We remove events that satisfy $\Delta m(K^+K^-\pi^+) < 0.15$ GeV$/c^2$. The surviving events still show a $D^0 \to K^+K^-$ signal which does not come from this D^{*+} decay. We remove events that satisfy $m(K^+K^-) > 1.85$ GeV$/c^2$.

Particle misidentification, in which a pion $\pi^+_{\rm mis}$ is wrongly identified as a kaon, is tested by assigning the pion mass to the K^+. In this way we identify the background due to the decay $D^+ \to K^-\pi^+\pi^+$ which, for the most part, populates the higher mass $D_s^+ \to K^+K^-\pi^+$ sideband. However, this cannot be removed without biasing the D_s^+ Dalitz plot, and so this background is taken into account in the Dalitz plot analysis.

We also observe a clean peak in the distribution of the mass difference $m(K^-\pi^+_{\rm mis}\pi^+) - m(K^-\pi^+_{\rm mis})$. Combining $m(K^-\pi^+_{\rm mis})$ with each of the π^0 meson candidates in the event, we identify this contamination as due to $D^{*+} \to \pi^+ D^0(\to K^-\pi^+\pi^0)$ with a missing π^0. We remove events that satisfy $m(K^-\pi^+_{\rm mis}\pi^+) - m(K^-\pi^+_{\rm mis}) < 0.15$ GeV$/c^2$.

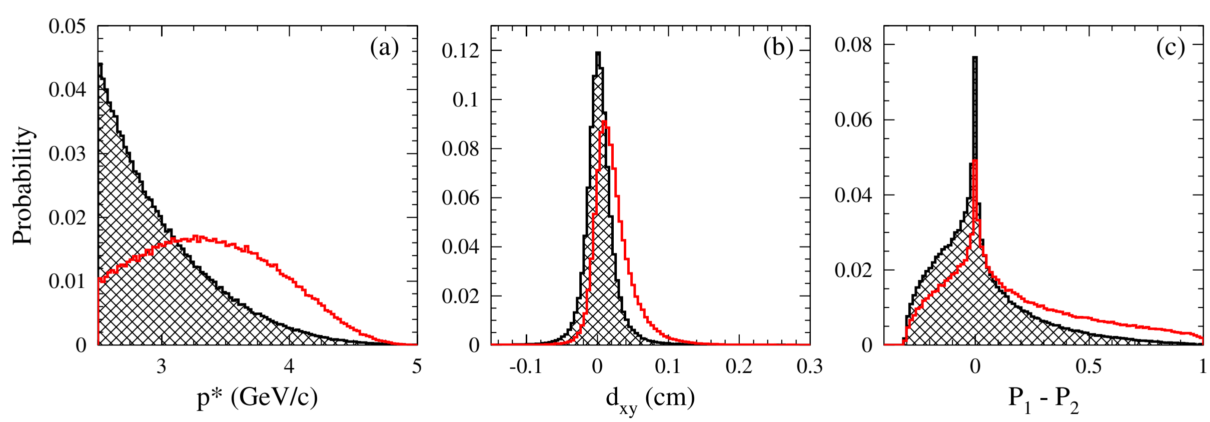

FIG. 1 (color online). Normalized probability distribution functions for signal (solid) and background events (hatched) used in a likelihood-ratio test for the event selection of $D_s^+ \to K^+K^-\pi^+$: (a) the center-of-mass momentum p^*, (b) the signed decay distance d_{xy}, and (c) the difference in probability $P_1 - P_2$.

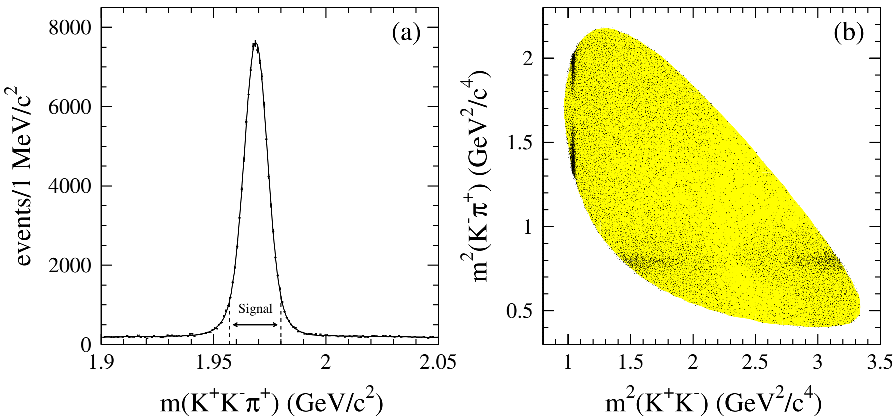

FIG. 2 (color online). (a) $K^+K^-\pi^+$ mass distribution for the D_s^+ analysis sample; the signal region is as indicated; (b) $D_s^+ \to K^+K^-\pi^+$ Dalitz plot.

Finally, we remove the D_s^+ candidates that share one or two daughters with another D_s^+ candidate; this reduces the number of candidates by 1.8%, corresponding to 0.9% of events. We allow there to be two or more nonoverlapping multiple candidates in the same event. The resulting $K^+K^-\pi^+$ mass distribution is shown in Fig. 2(a). This distribution is fitted with a double-Gaussian function for the signal, and a linear background. The fit gives a D_s^+ mass of $1968.70 \pm 0.02_{\mathrm{stat}}$ MeV$/c^2$, $\sigma_1 = 4.96 \pm 0.06_{\mathrm{stat}}$ MeV$/c^2$, $\sigma_2/\sigma_1 = 1.91 \pm 0.06_{\mathrm{stat}}$ where σ_1 (σ_2) is the standard deviation of the first (second) Gaussian, and errors are statistical only. The fractions of the two Gaussians are $f_{\sigma_1} = 0.80 \pm 0.02$ and $f_{\sigma_2} = 0.20 \pm 0.02$. The signal region is defined to be within $\pm 2\sigma_{D_s^+}$ of the fitted mass value, where $\sigma_{D_s^+} = \sqrt{f_{\sigma_1}\sigma_1^2 + f_{\sigma_2}\sigma_2^2} = 6.1$ MeV$/c^2$ is the observed mass resolution (the simulated mass resolution is 6 MeV$/c^2$). The number of signal events in this region (Signal), and the corresponding purity [defined as Signal/(Signal + Background)], are given in Table I.

For events in the $D_s^+ \to K^+K^-\pi^+$ signal region, we obtain the Dalitz plot shown in Fig. 2(b). For this distribution, and for the Dalitz plot analysis (Sec. VI), we use the track parameters obtained from the D_s^+ mass-constrained fit, since this yields a unique Dalitz plot boundary.

In the K^+K^- threshold region, a strong $\phi(1020)$ signal is observed, together with a rather broad structure. The $f_0(980)$ and $a_0(980)$ $\mathcal{S}$-wave resonances are, in fact, close to the K^+K^- threshold, and might be expected to contribute in the vicinity of the $\phi(1020)$. A strong $\bar{K}^*(892)^0$ signal can also be seen in the $K^-\pi^+$ system, but there is no evidence of structure in the $K^+\pi^+$ mass.

TABLE I. Yields and purities for the different D_s^+ decay modes. Quoted uncertainties are statistical only.

D_s^+ decay mode	Signal yield	Purity (%)
$K^+K^-\pi^+$	96307 ± 369	95
$K^+K^-K^+$	748 ± 60	28
$K^+K^+\pi^-$	356 ± 52	23

IV. EFFICIENCY

The selection efficiency for each D_s^+ decay mode analyzed is determined from a sample of Monte Carlo (MC) events in which the D_s^+ decay is generated according to phase space (i.e. such that the Dalitz plot is uniformly populated). The generated events are passed through a detector simulation based on the GEANT4 toolkit [14], and subjected to the same reconstruction and event selection procedure as that applied to the data. The distribution of the selected events in each Dalitz plot is then used to determine the reconstruction efficiency. The MC samples used to compute these efficiencies consist of 4.2×10^6 generated events for $D_s^+ \to K^+K^-\pi^+$ and $D_s^+ \to K^+K^+\pi^-$, and 0.7×10^6 for $D_s^+ \to K^+K^-K^+$.

For $D_s^+ \to K^+K^-\pi^+$, the efficiency distribution is fitted to a third-order polynomial in two dimensions using the expression,

$$\eta(x, y) = a_0 + a_1 x' + a_3 x'^2 + a_4 y'^2 + a_5 x' y' + a_6 x'^3 + a_7 y'^3, \tag{6}$$

where $x = m^2(K^+K^-)$, $y = m^2(K^-\pi^+)$, $x' = x - 2$, and $y' = y - 1.25$. Coefficients consistent with zero have been omitted. We obtain a good description of the efficiency with $\chi^2/\mathrm{NDF} = 1133/(1147 - 7) = 0.994$ (where NDF refers to the number of degrees of freedom). The efficiency is found to be almost uniform in $K^-\pi^+$ and K^+K^- mass, with an average value of $\approx 3.3\%$ (Fig. 3).

V. PARTIAL-WAVE ANALYSIS OF THE K^+K^- AND $K^-\pi^+$ THRESHOLD REGIONS

In the K^+K^- threshold region both $a_0(980)$ and $f_0(980)$ can be present, and both resonances have very similar parameters which suffer from large uncertainties. In this

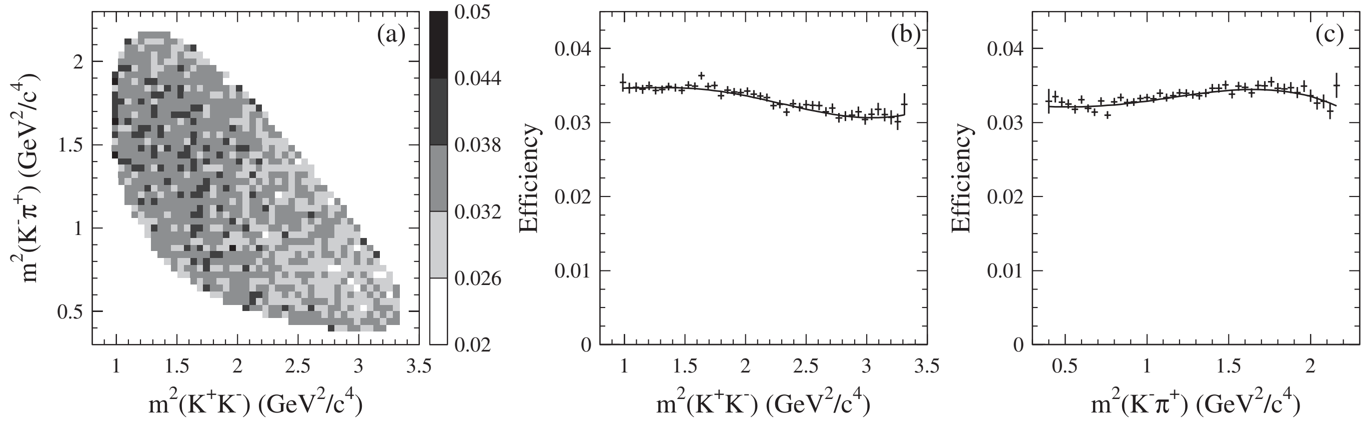

FIG. 3. (a) Dalitz plot efficiency map; the projection onto (b) the K^+K^-, and (c) the $K^-\pi^+$ axis.

section we obtain model-independent information on the K^+K^- $\mathcal{S}$ wave by performing a partial-wave analysis in the K^+K^- threshold region.

Let N be the number of events for a given mass interval $I = [m_{K^+K^-}; m_{K^+K^-} + dm_{K^+K^-}]$. We write the corresponding angular distribution in terms of the appropriate spherical harmonic functions as

$$\frac{dN}{d\cos\theta} = 2\pi \sum_{k=0}^{L} \langle Y_k^0 \rangle Y_k^0(\cos\theta), \tag{7}$$

where $L = 2\ell_{\max}$, and $\ell_{\max}$ is the maximum orbital angular momentum quantum number required to describe the K^+K^- system at $m_{K^+K^-}$ (e.g. $\ell_{\max} = 1$ for an $\mathcal{S}$-, $\mathcal{P}$-wave description); θ is the angle between the K^+ direction in the K^+K^- rest frame and the prior direction of the K^+K^- system in the D_s^+ rest frame. The normalizations are such that

$$\int_{-1}^{1} Y_k^0(\cos\theta) Y_j^0(\cos\theta) d\cos\theta = \frac{\delta_{kj}}{2\pi}, \tag{8}$$

and it is assumed that the distribution $\frac{dN}{d\cos\theta}$ has been efficiency corrected and background subtracted.

Using this orthogonality condition, the coefficients in the expansion are obtained from

$$\langle Y_k^0 \rangle = \int_{-1}^{1} Y_k^0(\cos\theta) \frac{dN}{d\cos\theta} d\cos\theta, \tag{9}$$

where the integral is given, to a good approximation, by $\sum_{n=1}^{N} Y_k^0(\cos\theta_n)$, where θ_n is the value of θ for the n-th event.

Figure 4 shows the K^+K^- mass spectrum up to $1.5\ \mathrm{GeV}/c^2$ weighted by $Y_k^0(\cos\theta) = \sqrt{(2k+1)/4\pi} P_k(\cos\theta)$ for $k = 0$, 1, and 2, where P_k is the Legendre polynomial function of order k. These distributions are corrected for efficiency and phase space, and background is subtracted using the D_s^+ sidebands.

The number of events N for the mass interval I can be expressed also in terms of the partial-wave amplitudes describing the K^+K^- system. Assuming that only $\mathcal{S}$- and $\mathcal{P}$-wave amplitudes are necessary in this limited region, we can write:

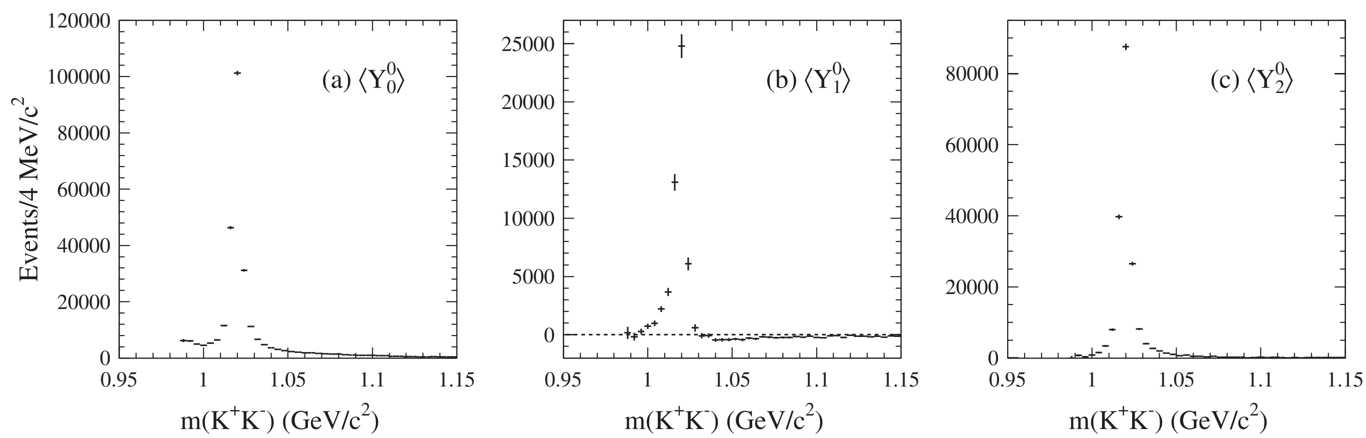

FIG. 4. K^+K^- mass spectrum in the threshold region weighted by (a) Y_0^0, (b) Y_1^0, and (c) Y_2^0, corrected for efficiency and phase space, and background subtracted.

$$\frac{dN}{d\cos\theta} = 2\pi|\mathcal{S}Y_0^0(\cos\theta) + \mathcal{P}Y_1^0(\cos\theta)|^2. \tag{10}$$

By comparing Eqs. (7) and (10) [15], we obtain

$$\begin{aligned}
\sqrt{4\pi}\langle Y_0^0\rangle &= |\mathcal{S}|^2 + |\mathcal{P}|^2,\\
\sqrt{4\pi}\langle Y_1^0\rangle &= 2|\mathcal{S}||\mathcal{P}|\cos\phi_{\mathcal{SP}},\\
\sqrt{4\pi}\langle Y_2^0\rangle &= \frac{2}{\sqrt{5}}|\mathcal{P}|^2,
\end{aligned} \tag{11}$$

where $\phi_{\mathcal{SP}} = \phi_{\mathcal{S}} - \phi_{\mathcal{P}}$ is the phase difference between the $\mathcal{S}$- and $\mathcal{P}$-wave amplitudes. These equations relate the interference between the $\mathcal{S}$ wave [$f_0(980)$, and/or $a_0(980)$, and/or nonresonant] and the $\mathcal{P}$ wave [$\phi(1020)$] to the prominent structure in $\langle Y_1^0\rangle$ [Fig. 4(b)]. The $\langle Y_1^0\rangle$ distribution shows the same behavior as for $D_s^+ \to K^+K^-e^+\nu_e$ decay [16]. The $\langle Y_2^0\rangle$ distribution [Fig. 4(c)], on the other hand, is consistent with the $\phi(1020)$ line shape.

The above system of equations can be solved in each interval of K^+K^- invariant mass for $|\mathcal{S}|$, $|\mathcal{P}|$, and $\phi_{\mathcal{SP}}$, and the resulting distributions are shown in Fig. 5. We observe a threshold enhancement in the $\mathcal{S}$ wave [Fig. 5(a)], and the expected $\phi(1020)$ Breit-Wigner (BW) in the $\mathcal{P}$ wave [Fig. 5(b)]. We also observe the expected $\mathcal{S}$-$\mathcal{P}$ relative phase motion in the $\phi(1020)$ region [Fig. 5(c)].

A. $\mathcal{P}$-wave/$\mathcal{S}$-wave ratio in the $\phi(1020)$ region

The decay mode $D_s^+ \to \phi(1020)\pi^+$ is used often as the normalizing mode for D_s^+ decay branching fractions, typically by selecting a K^+K^- invariant mass region around the $\phi(1020)$ peak. The observation of a significant $\mathcal{S}$-wave contribution in the threshold region means that this contribution must be taken into account in such a procedure.

In this section we estimate the $\mathcal{P}$-wave/$\mathcal{S}$-wave ratio in an almost model-independent way. In fact integrating the distributions of $\sqrt{4\pi}pq'\langle Y_0^0\rangle$ and $\sqrt{5\pi}pq'\langle Y_2^0\rangle$ (Fig. 4) in a region around the $\phi(1020)$ peak yields $\int(|\mathcal{S}|^2 + |\mathcal{P}|^2)pq'dm_{K^+K^-}$ and $\int|\mathcal{P}|^2pq'dm_{K^+K^-}$, respectively, where p is the K^+ momentum in the K^+K^- rest frame, and q' is the momentum of the bachelor π^+ in the D_s^+ rest frame.

The $\mathcal{S}$-$\mathcal{P}$ interference contribution integrates to zero, and we define the $\mathcal{P}$-wave and $\mathcal{S}$-wave fractions as

$$f_{\mathcal{P}\text{-wave}} = \frac{\int|\mathcal{P}|^2pq'dm_{K^+K^-}}{\int(|\mathcal{S}|^2 + |\mathcal{P}|^2)pq'dm_{K^+K^-}}, \tag{12}$$

$$f_{\mathcal{S}\text{-wave}} = \frac{\int|\mathcal{S}|^2pq'dm_{K^+K^-}}{\int(|\mathcal{S}|^2 + |\mathcal{P}|^2)pq'dm_{K^+K^-}} = 1 - f_{\mathcal{P}\text{-wave}}. \tag{13}$$

The experimental mass resolution is estimated by comparing generated and reconstructed MC events, and is $\simeq 0.5\ \text{MeV}/c^2$ at the ϕ mass peak. Table II gives the

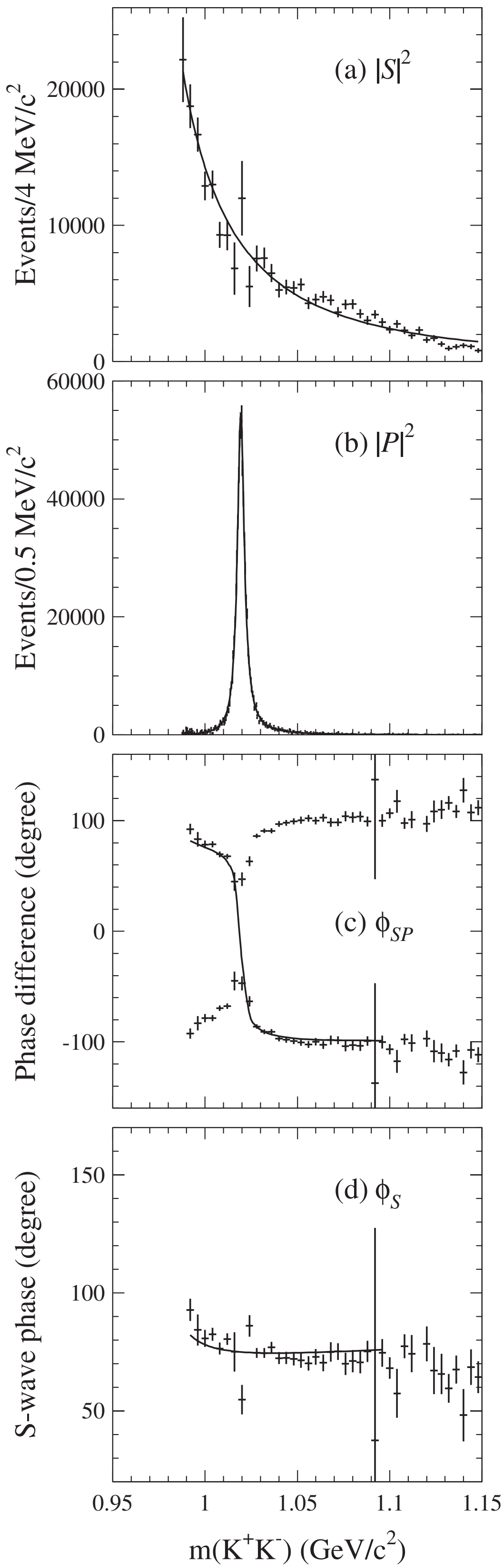

FIG. 5. Squared (a) $\mathcal{S}$- and (b) $\mathcal{P}$-wave amplitudes; (c) the phase difference $\phi_{\mathcal{SP}}$; (d) $\phi_{\mathcal{S}}$ obtained as explained in the text. The curves result from the fit described in the text.

resulting $\mathcal{S}$-wave and $\mathcal{P}$-wave fractions computed for three K^+K^- mass regions. The last column of Table II shows the measurements of the relative overall rate ($\frac{N}{N_{\rm tot}}$) defined as the number of events in the K^+K^- mass interval over the number of events in the entire Dalitz plot after efficiency-correction and background-subtraction.

B. $\mathcal{S}$-wave parametrization at the K^+K^- threshold

In this section we extract a phenomenological description of the $\mathcal{S}$ wave assuming that it is dominated by the $f_0(980)$ resonance while the $\mathcal{P}$ wave is described entirely by the $\phi(1020)$ resonance. We also assume that no other contribution is present in this limited region of the Dalitz plot. We therefore perform a simultaneous fit of the three distributions shown in Figs. 5(a)–5(c) using the following model:

$$\begin{aligned} \frac{dN_{\mathcal{S}^2}}{dm_{K^+K^-}} &= |C_{f_0(980)}A_{f_0(980)}|^2, \\ \frac{dN_{\mathcal{P}^2}}{dm_{K^+K^-}} &= |C_{\phi}A_{\phi}|^2, \\ \frac{dN_{\phi_{\mathcal{S}\mathcal{P}}}}{dm_{K^+K^-}} &= arg(A_{f_0(980)}e^{i\delta}) - arg(A_{\phi}), \end{aligned} \tag{14}$$

where C_{ϕ}, $C_{f_0(980)}$, and δ are free parameters and

$$A_{\phi} = \frac{F_rF_D}{m_{\phi}^2 - m^2 - im_{\phi}\Gamma} \times 4pq \tag{15}$$

is the spin 1 relativistic BW parametrizing the $\phi(1020)$ with Γ expressed as

$$\Gamma = \Gamma_r\left(\frac{p}{p_r}\right)^{2J+1}\left(\frac{M_r}{m}\right)F_r^2. \tag{16}$$

Here q is the momentum of the bachelor π^+ in the K^+K^- rest frame. The parameters in Eqs. (15) and (16) are defined in Sec. VI below.

For $A_{f_0(980)}$ we first tried a coupled channel BW (Flatté) amplitude [17]. However, we find that this parametrization is insensitive to the coupling to the $\pi\pi$ channel. Therefore, we empirically parametrize the $f_0(980)$ with the following function:

$$A_{f_0(980)} = \frac{1}{m_0^2 - m^2 - im_0\Gamma_0\rho_{KK}}, \tag{17}$$

TABLE II. $\mathcal{S}$-wave and $\mathcal{P}$-wave fractions computed in three K^+K^- mass ranges around the $\phi(1020)$ peak. Errors are statistical only.

$m_{K^+K^-}$ (MeV/c^2)	$f_{\mathcal{S}\text{-wave}}$ (%)	$f_{\mathcal{P}\text{-wave}}$ (%)	$\frac{N}{N_{\rm tot}}$ (%)
1019.456 ± 5	3.5 ± 1.0	96.5 ± 1.0	29.4 ± 0.2
1019.456 ± 10	5.6 ± 0.9	94.4 ± 0.9	35.1 ± 0.2
1019.456 ± 15	7.9 ± 0.9	92.1 ± 0.9	37.8 ± 0.2

where $\rho_{KK} = 2p/m$, and obtains the following parameter values:

$$\begin{aligned} m_0 &= (0.922 \pm 0.003_{\rm stat})\ {\rm GeV}/c^2, \\ \Gamma_0 &= (0.24 \pm 0.08_{\rm stat})\ {\rm GeV}. \end{aligned} \tag{18}$$

The errors are statistical only. The fit results are superimposed on the data in Fig. 5.

In Fig. 5(c), the $\mathcal{S}$-$\mathcal{P}$ phase difference is plotted twice because of the sign ambiguity associated with the value of $\phi_{\mathcal{S}\mathcal{P}}$ extracted from $\cos\phi_{\mathcal{S}\mathcal{P}}$. We can extract the mass-dependent $f_0(980)$ phase by adding the mass-dependent $\phi(1020)$ BW phase to the $\phi_{\mathcal{S}\mathcal{P}}$ distributions of Fig. 5(c). Since the K^+K^- mass region is significantly above the $f_0(980)$ central mass value of Eq. (18), we expect that the $\mathcal{S}$-wave phase will be moving much more slowly in this region than in the $\phi(1020)$ region. Consequently, we resolve the phase ambiguity of Fig. 5(c) by choosing as the physical solution the one which decreases rapidly in the $\phi(1020)$ peak region, since this reflects the rapid forward BW phase motion associated with a narrow resonance. The result is shown in Fig. 5(d), where we see that the $\mathcal{S}$-wave phase is roughly constant, as would be expected for the tail of a resonance. The slight decrease observed with increasing mass might be due to higher mass contributions to the $\mathcal{S}$-wave amplitude. The values of $|\mathcal{S}|^2$ (arbitrary units) and phase values are reported in Table III, together with the corresponding values of $|\mathcal{P}|^2$.

In Fig. 6(a) we compare the $\mathcal{S}$-wave profile from this analysis with the $\mathcal{S}$-wave intensity values extracted from Dalitz plot analyses of $D^0 \to \bar{K}^0K^+K^-$ [18] and $D^0 \to K^+K^-\pi^0$ [19]. The four distributions are normalized in the region from threshold up to 1.05 GeV/c^2. We observe substantial agreement. As the $a_0(980)$ and $f_0(980)$ mesons couple mainly to the $u\bar{u}/d\bar{d}$ and $s\bar{s}$ systems, respectively, the former is favored in $D^0 \to \bar{K}^0K^+K^-$ and the latter in $D_s^+ \to K^+K^-\pi^+$. Both resonances can contribute in $D^0 \to K^+K^-\pi^0$. We conclude that the $\mathcal{S}$-wave projections in the $K\bar{K}$ system for both resonances are consistent in shape. It has been suggested that this feature supports the hypothesis that the $a_0(980)$ and $f_0(980)$ are 4-quark states [20]. We also compare the $\mathcal{S}$-wave profile from this analysis with the $\pi^+\pi^-$ $\mathcal{S}$-wave profile extracted from *BABAR* data in a Dalitz plot analysis of $D_s^+ \to \pi^+\pi^-\pi^+$ [4] [Fig. 6(b)]. The observed agreement supports the argument that only the $f_0(980)$ is present in this limited mass region.

C. Study of the $K^-\pi^+$ $\mathcal{S}$ wave at threshold

We perform a model-independent analysis, similar to that described in the previous sections, to extract the $K\pi$ $\mathcal{S}$-wave behavior as a function of mass in the threshold region up to 1.1 GeV/c^2. Figure 7 shows the $K^-\pi^+$ mass spectrum in this region, weighted by $Y_k^0(\cos\theta) = \sqrt{(2k+1)/4\pi}P_k(\cos\theta)$, with $k = 0$, 1, and 2, corrected

TABLE III. $\mathcal{S}$- and $\mathcal{P}$-wave squared amplitudes (in arbitrary units) and the $\mathcal{S}$-wave phase. The $\mathcal{S}$-wave phase values, corresponding to the mass 0.988 and 1.116 GeV/c^2, are missing because the $\langle Y_2^0\rangle$ distribution [Fig. 4(c)] goes negative or $|\cos\phi_{\mathcal{SP}}| > 1$ and so Eqs. (11) cannot be solved. Quoted uncertainties are statistical only.

$m_{K^+K^-}$ (GeV/c^2)	$\lvert\mathcal{S}\rvert^2$ (arbitrary units)	$\lvert\mathcal{P}\rvert^2$ (arbitrary units)	$\phi_{\mathcal{S}}$ (degrees)
0.988	22178 ± 3120	-133 ± 2283	
0.992	18760 ± 1610	2761 ± 1313	92 ± 5
0.996	16664 ± 1264	1043 ± 971	84 ± 7
1	12901 ± 1058	3209 ± 882	81 ± 4
1.004	13002 ± 1029	5901 ± 915	82 ± 3
1.008	9300 ± 964	13484 ± 1020	76 ± 3
1.012	9287 ± 1117	31615 ± 1327	80 ± 2
1.016	6829 ± 1930	157412 ± 2648	75 ± 8
1.02	11987 ± 2734	346890 ± 3794	55 ± 6
1.024	5510 ± 1513	104892 ± 2055	86 ± 5
1.028	7565 ± 952	32239 ± 1173	75 ± 2
1.032	7596 ± 768	15899 ± 861	74 ± 2
1.036	6497 ± 658	10399 ± 707	77 ± 2
1.04	5268 ± 574	7638 ± 609	72 ± 3
1.044	5467 ± 540	5474 ± 540	72 ± 3
1.048	5412 ± 506	4026 ± 483	72 ± 3
1.052	5648 ± 472	2347 ± 423	71 ± 3
1.056	4288 ± 442	3056 ± 421	70 ± 3
1.06	4548 ± 429	1992 ± 384	73 ± 3
1.064	4755 ± 425	1673 ± 374	70 ± 4
1.068	4508 ± 393	1074 ± 334	75 ± 4
1.072	3619 ± 373	1805 ± 345	75 ± 4
1.076	4189 ± 368	840 ± 312	70 ± 5
1.08	4215 ± 367	770 ± 297	71 ± 5
1.084	3508 ± 345	866 ± 294	71 ± 5
1.088	3026 ± 322	929 ± 285	75 ± 4
1.092	3456 ± 309	79 ± 240	37 ± 90
1.096	2903 ± 300	488 ± 256	75 ± 6
1.1	2335 ± 282	885 ± 248	68 ± 5
1.104	2761 ± 284	341 ± 231	57 ± 10
1.108	2293 ± 273	602 ± 231	77 ± 5
1.112	1913 ± 238	269 ± 186	74 ± 8
1.116	2325 ± 252	57 ± 198	
1.12	1596 ± 228	308 ± 194	78 ± 7
1.124	1707 ± 224	233 ± 188	67 ± 10
1.128	1292 ± 207	270 ± 176	66 ± 9
1.132	969 ± 197	586 ± 172	60 ± 6
1.136	1092 ± 196	553 ± 170	67 ± 6
1.14	1180 ± 193	316 ± 167	48 ± 11
1.144	1107 ± 187	354 ± 170	68 ± 8
1.148	818 ± 178	521 ± 164	64 ± 7

for efficiency, phase space, and with background from the D_s^+ sidebands subtracted; θ is the angle between the K^- direction in the $K^-\pi^+$ rest frame and the prior direction of the $K^-\pi^+$ system in the D_s^+ rest frame. We observe that $\langle Y_0^0\rangle$ and $\langle Y_2^0\rangle$ show strong $\bar{K}^*(892)^0$ resonance signals, and that the $\langle Y_1^0\rangle$ moment shows evidence for $\mathcal{S}$-$\mathcal{P}$ interference.

We use Eqs. (11) to solve for $|\mathcal{S}|$ and $|\mathcal{P}|$. The result for the $\mathcal{S}$ wave is shown in Fig. 7(d). We observe a small $\mathcal{S}$-wave contribution which does not allow us to measure the expected phase motion relative to that of the $\bar{K}^*(892)^0$ resonance. Indeed, the fact that $|\mathcal{S}|^2$ goes negative indicates that a model including only $\mathcal{S}$- and $\mathcal{P}$-wave components is not sufficient to describe the $K^-\pi^+$ system.

VI. DALITZ PLOT FORMALISM

An unbinned maximum likelihood fit is performed in which the distribution of events in the Dalitz plot is used to

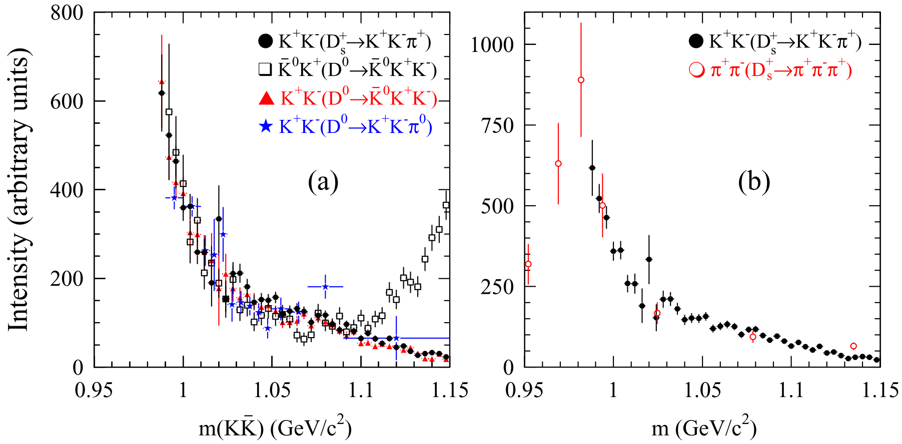

FIG. 6 (color online). (a) Comparison between $K\bar{K}$ $\mathcal{S}$-wave intensities from different charmed meson Dalitz plot analyses. (b) Comparison of the $K\bar{K}$ $\mathcal{S}$-wave intensity from $D_s^+ \to K^+K^-\pi^+$ with the $\pi^+\pi^-$ $\mathcal{S}$-wave intensity from $D_s^+ \to \pi^+\pi^-\pi^+$.

determine the relative amplitudes and phases of intermediate resonant and nonresonant states.

The likelihood function is written as

$$\mathcal{L} = \prod_{n=1}^{N}\Bigg[f_{\text{sig}} \cdot \eta(x, y) \frac{\sum_{i,j} c_i c_j^* A_i(x, y) A_j^*(x, y)}{\sum_{i,j} c_i c_j^* I_{A_i A_j^*}} + (1 - f_{\text{sig}}) \frac{\sum_i k_i B_i(x, y)}{\sum_i k_i I_{B_i}}\Bigg], \tag{19}$$

where

(i) N is the number of events in the signal region;
(ii) $x = m^2(K^+K^-)$ and $y = m^2(K^-\pi^+)$;
(iii) f_{sig} is the fraction of signal as a function of the $K^+K^-\pi^+$ invariant mass, obtained from the fit to the $K^+K^-\pi^+$ mass spectrum [Fig. 2(a)];
(iv) $\eta(x, y)$ is the efficiency, parametrized by a third order polynomial (Sec. IV);
(v) the $A_i(x, y)$ describe the complex signal amplitude contributions;
(vi) the $B_i(x, y)$ describe the background probability density function contributions;
(vii) k_i is the magnitude of the i-th component for the background. The k_i parameters are obtained by fitting the sideband regions;
(viii) $I_{A_i A_j^*} = \int A_i(x, y) A_j^*(x, y) \eta(x, y) dxdy$ and $I_{B_i} = \int B_i(x, y) dxdy$ are normalization integrals. Numerical integration is performed by means of Gaussian quadrature [21];
(ix) c_i is the complex amplitude of the i-th component for the signal. The c_i parameters are allowed to vary during the fit process.

The phase of each amplitude (i.e. the phase of the corresponding c_i) is measured with respect to the $K^+\bar{K}^*(892)^0$ amplitude. Following the method described in Ref. [22], each amplitude $A_i(x, y)$ is represented by the product of a complex BW and a real angular term T depending on the solid angle Ω:

$$A(x, y) = BW(m) \times T(\Omega). \tag{20}$$

For a D_s meson decaying into three pseudoscalar mesons via an intermediate resonance r ($D_s \to rC$, $r \to AB$), $BW(M_{AB})$ is written as a relativistic BW:

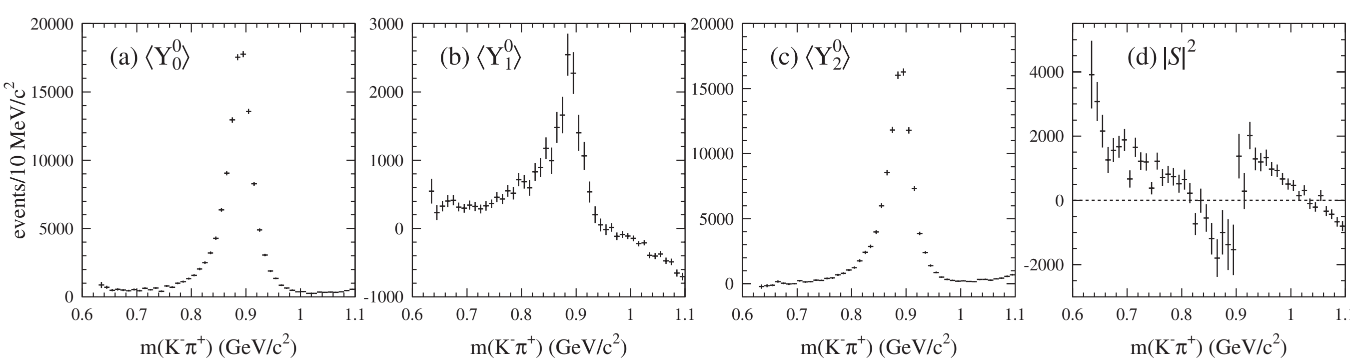

FIG. 7. $K^-\pi^+$ mass spectrum in the threshold region weighted by (a) Y_0^0, (b) Y_1^0, and (c) Y_2^0, corrected for efficiency, phase space, and background subtracted. (d) The $K^-\pi^+$ mass dependence of $|\mathcal{S}|^2$.

$$BW(M_{AB}) = \frac{F_r F_D}{M_r^2 - M_{AB}^2 - i\Gamma_{AB} M_r}, \tag{21}$$

where Γ_{AB} is a function of the invariant mass of system AB (M_{AB}), the momentum p_{AB} of either daughter in the AB rest frame, the spin J of the resonance and the mass M_r, and the width Γ_r of the resonance. The explicit expression is

$$\Gamma_{AB} = \Gamma_r \left(\frac{p_{AB}}{p_r}\right)^{2J+1} \left(\frac{M_r}{M_{AB}}\right) F_r^2, \tag{22}$$

$$p_{AB} = \frac{\sqrt{(M_{AB}^2 - M_A^2 - M_B^2)^2 - 4M_A^2 M_B^2}}{2M_{AB}}. \tag{23}$$

The form factors F_r and F_D attempt to model the underlying quark structure of the parent particle and the intermediate resonances. We use the Blatt-Weisskopf penetration factors [23] (Table IV), which depend on a single parameter R representing the meson "radius." We assume $R_{D_s^+} = 3\ \text{GeV}^{-1}$ for the D_s and $R_r = 1.5\ \text{GeV}^{-1}$ for the intermediate resonances; q_{AB} is the momentum of the bachelor C in the AB rest frame:

$$q_{AB} = \frac{\sqrt{(M_{D_s}^2 + M_C^2 - M_{AB}^2)^2 - 4M_{D_s}^2 M_C^2}}{2M_{AB}}. \tag{24}$$

p_r and q_r are the values of p_{AB} and q_{AB} when $m_{AB} = m_r$.

The angular terms $T(\Omega)$ are described by the following expressions:

$$\begin{aligned}
&\text{Spin 0: } T(\Omega) = 1,\\
&\text{Spin 1: } T(\Omega) = M_{BC}^2 - M_{AC}^2 - \frac{(M_{D_s}^2 - M_C^2)(M_B^2 - M_A^2)}{M_{AB}^2},\\
&\text{Spin 2: } T(\Omega) = a_1^2 - \frac{1}{3} a_2 a_3,
\end{aligned} \tag{25}$$

where

TABLE IV. Summary of the Blatt-Weisskopf penetration form factors. q_r and p_r are the momenta of the decay particles in the parent rest frame.

Spin	F_r	F_D
0	1	1
1	$\frac{\sqrt{1+(R_r p_r)^2}}{\sqrt{1+(R_r p_{AB})^2}}$	$\frac{\sqrt{1+(R_{D_s^+} q_r)^2}}{\sqrt{1+(R_{D_s^+} q_{AB})^2}}$
2	$\frac{\sqrt{9+3(R_r p_r)^2+(R_r p_r)^4}}{\sqrt{9+3(R_r p_{AB})^2+(R_r p_{AB})^4}}$	$\frac{\sqrt{9+3(R_{D_s^+} q_r)^2+(R_{D_s^+} q_r)^4}}{\sqrt{9+3(R_{D_s^+} q_{AB})^2+(R_{D_s^+} q_{AB})^4}}$

$$\begin{aligned}
a_1 &= M_{BC}^2 - M_{AC}^2 + \frac{(M_{D_s}^2 - M_C^2)(M_A^2 - M_B^2)}{M_{AB}^2},\\
a_2 &= M_{AB}^2 - 2M_{D_s}^2 - 2M_C^2 + \frac{(M_{D_s}^2 - M_C^2)^2}{M_{AB}^2},\\
a_3 &= M_{AB}^2 - 2M_A^2 - 2M_B^2 + \frac{(M_A^2 - M_B^2)^2}{M_{AB}^2}.
\end{aligned} \tag{26}$$

Resonances are included in sequence, starting from those immediately visible in the Dalitz plot projections. All allowed resonances from Ref. [10] have been tried, and we reject those with amplitudes consistent with zero. The goodness of fit is tested by an adaptive binning χ^2.

The efficiency-corrected fractional contribution due to the resonant or nonresonant contribution i is defined as follows:

$$f_i = \frac{|c_i|^2 \int |A_i(x,y)|^2 dxdy}{\int |\sum_j c_j A_j(x,y)|^2 dxdy}. \tag{27}$$

The f_i do not necessarily add to 1 because of interference effects. We also define the interference fit fraction between the resonant or nonresonant contributions k and l as:

$$f_{kl} = \frac{2\int \Re[c_k c_l^* A_k(x,y) A_l^*(x,y)] dxdy}{\int |\sum_j c_j A_j(x,y)|^2 dxdy}. \tag{28}$$

Note that $f_{kk} = 2f_k$. The error on each f_i and f_{kl} is evaluated by propagating the full covariance matrix obtained from the fit.

Background parametrization

To parametrize the D_s^+ background, we use the D_s^+ sideband regions. An unbinned maximum likelihood fit is performed using the function:

$$\mathcal{L} = \prod_{n=1}^{N_B} \left[\frac{\sum_i k_i B_i}{\sum_i k_i I_{B_i}}\right], \tag{29}$$

where N_B is the number of sideband events, the k_i parameters are real coefficients floated in the fit, and the B_i parameters represent Breit-Wigner functions that are summed incoherently.

The Dalitz plot for the two sidebands shows the presence of $\phi(1020)$ and $\bar{K}^*(892)^0$ (Fig. 8). There are further structures not clearly associated with known resonances and due to reflections of other final states. Since they do not have definite spin, we parametrize the background using an incoherent sum of $\mathcal{S}$-wave Breit-Wigner shapes.

VII. DALITZ PLOT ANALYSIS OF $D_s^+ \to K^+K^-\pi^+$

Using the method described in Sec. VI, we perform an unbinned maximum likelihood fit to the $D_s^+ \to K^+K^-\pi^+$ decay channel. The fit is performed in steps, by adding

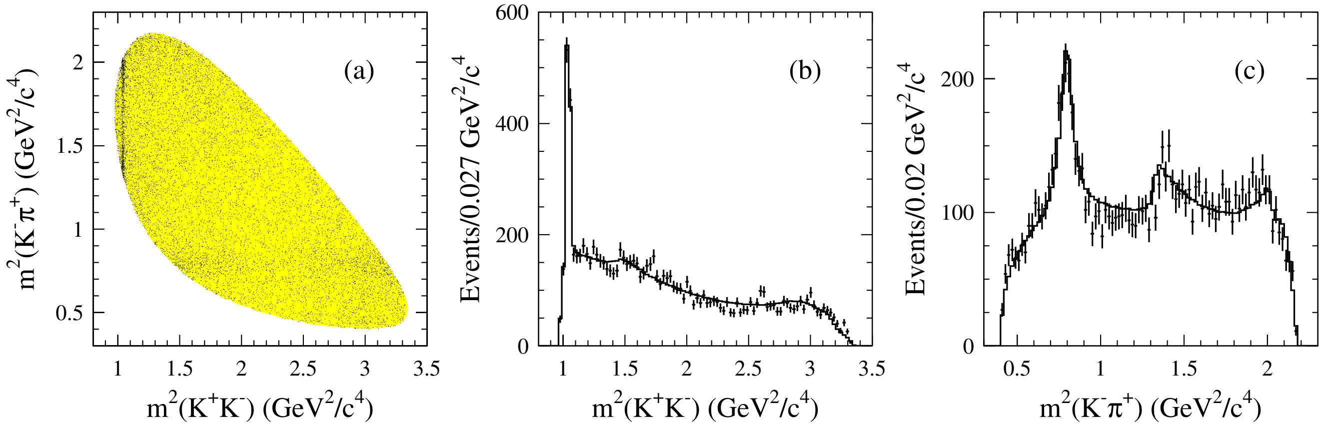

FIG. 8 (color online). (a) Dalitz plot of sideband regions projected onto (b) the K^+K^- and (c) the $K^-\pi^+$ axis.

resonances one after the other. Most of the masses and widths of the resonances are taken from Ref. [10]. For the $f_0(980)$ we use the phenomenological model described in Sec. V B. The $\bar{K}^*(892)^0$ amplitude is chosen as the reference amplitude.

The decay fractions, amplitudes, and relative phase values for the best fit obtained, are summarized in Table V where the first error is statistical, and the second is systematic. The interference fractions are quoted in Table VI where the error is statistical only. We observe the following features.

(i) The decay is dominated by the $\bar{K}^*(892)^0K^+$ and $\phi(1020)\pi^+$ amplitudes.

(ii) The fit quality is substantially improved by leaving the $\bar{K}^*(892)^0$ parameters free in the fit. The fitted parameters are

$$m_{\bar{K}^*(892)^0} = (895.6 \pm 0.2_{\rm stat} \pm 0.3_{\rm sys})\ {\rm MeV}/c^2,$$
$$\Gamma_{\bar{K}^*(892)^0} = (45.1 \pm 0.4_{\rm stat} \pm 0.4_{\rm sys})\ {\rm MeV}. \quad (30)$$

We notice that the width is about 3 MeV lower than that in Ref. [10]. However this measurement is

TABLE V. Results from the $D_s^+ \to K^+K^-\pi^+$ Dalitz plot analysis. The table gives fit fractions, amplitudes, and phases from the best fit. Quoted uncertainties are statistical and systematic, respectively.

Decay mode	Decay function (%)	Amplitude	Phase (radians)
$\bar{K}^*(892)^0K^+$	$47.9 \pm 0.5 \pm 0.5$	1. (Fixed)	0. (Fixed)
$\phi(1020)\pi^+$	$41.4 \pm 0.8 \pm 0.5$	$1.15 \pm 0.01 \pm 0.26$	$2.89 \pm 0.02 \pm 0.04$
$f_0(980)\pi^+$	$16.4 \pm 0.7 \pm 2.0$	$2.67 \pm 0.05 \pm 0.20$	$1.56 \pm 0.02 \pm 0.09$
$\bar{K}_0^*(1430)^0K^+$	$2.4 \pm 0.3 \pm 1.0$	$1.14 \pm 0.06 \pm 0.36$	$2.55 \pm 0.05 \pm 0.22$
$f_0(1710)\pi^+$	$1.1 \pm 0.1 \pm 0.1$	$0.65 \pm 0.02 \pm 0.06$	$1.36 \pm 0.05 \pm 0.20$
$f_0(1370)\pi^+$	$1.1 \pm 0.1 \pm 0.2$	$0.46 \pm 0.03 \pm 0.09$	$-0.45 \pm 0.11 \pm 0.52$
Sum	$110.2 \pm 0.6 \pm 2.0$		
χ^2/NDF	$2843/(2305 - 14) = 1.24$		

TABLE VI. Fit fractions matrix of the best fit. The diagonal elements f_i correspond to the decay fractions in Table V. The off-diagonal elements give the fit fractions of the interference f_{kl}. The null values originate from the fact that any $\mathcal{S}$-$\mathcal{P}$ interference contribution integrates to zero. Quoted uncertainties are statistical only.

f_{kl} (%)	$\bar{K}^*(892)^0K^+$	$\phi(1020)\pi^+$	$f_0(980)\pi^+$	$\bar{K}_0^*(1430)^0K^+$	$f_0(1710)\pi^+$	$f_0(1370)\pi^+$
$\bar{K}^*(892)^0K^+$	47.9 ± 0.5	-4.36 ± 0.03	-2.4 ± 0.2	0.	-0.06 ± 0.03	0.08 ± 0.08
$\phi(1020)\pi^+$		41.4 ± 0.8	0.	-0.7 ± 0.2	0.	0.
$f_0(980)\pi^+$			16.4 ± 0.7	4.1 ± 0.6	-3.1 ± 0.2	-4.5 ± 0.3
$\bar{K}_0^*(1430)^0K^+$				2.4 ± 0.3	0.48 ± 0.08	-0.7 ± 0.1
$f_0(1710)\pi^+$					1.1 ± 0.1	0.86 ± 0.06
$f_0(1370)\pi^+$						1.1 ± 0.1

consistent with results from other Dalitz plot analyses [9].

(iii) The $f_0(1370)$ contribution is also left free in the fit, and we obtain the following parameter values:

$$m_{f_0(1370)} = (1.22 \pm 0.01_{\text{stat}} \pm 0.04_{\text{sys}})\ \text{GeV}/c^2,$$
$$\Gamma_{f_0(1370)} = (0.21 \pm 0.01_{\text{stat}} \pm 0.03_{\text{sys}})\ \text{GeV}. \quad (31)$$

These values are within the broad range of values measured by other experiments [10].

(iv) A nonresonant contribution, represented by a constant complex amplitude, was included in the fit function. However, this contribution was found to be consistent with zero, and therefore is excluded from the final fit function.

(v) In a similar way contributions from the $K_1^*(1410)$, $f_0(1500)$, $f_2(1270)$, and $f_2'(1525)$ are found to be consistent with zero.

(vi) The replacement of the $K_0^*(1430)$ by the LASS parametrization [24] of the entire $K\pi$ $\mathcal{S}$ wave does not improve the fit quality.

(vii) The fit does not require any contribution from the $\kappa(800)$ [1].

The results of the best fit [$\chi^2/\text{NDF} = 2843/(2305 - 14) = 1.24$] are superimposed on the Dalitz plot projections in Fig. 9. Other recent high statistics charm Dalitz plot analyses at *BABAR* [25] have shown that a significant contribution to the χ^2/NDF can arise from imperfections in modelling experimental effects. The normalized fit residuals shown under each distribution (Fig. 9) are given by Pull $= (N_{\text{data}} - N_{\text{fit}})/\sqrt{N_{\text{data}}}$. The data are well reproduced in all the projections. We observe some disagreement in the $K^-\pi^+$ projection below 0.5 GeV$^2/c^4$. It may be due to a poor parametrization of the background in this limited mass region. A systematic uncertainty takes such effects in account (Sec. VII A). The missing of a $K\pi$ $\mathcal{S}$-wave amplitude in the $K^-\pi^+$ low mass region may be also the source of such disagreement.

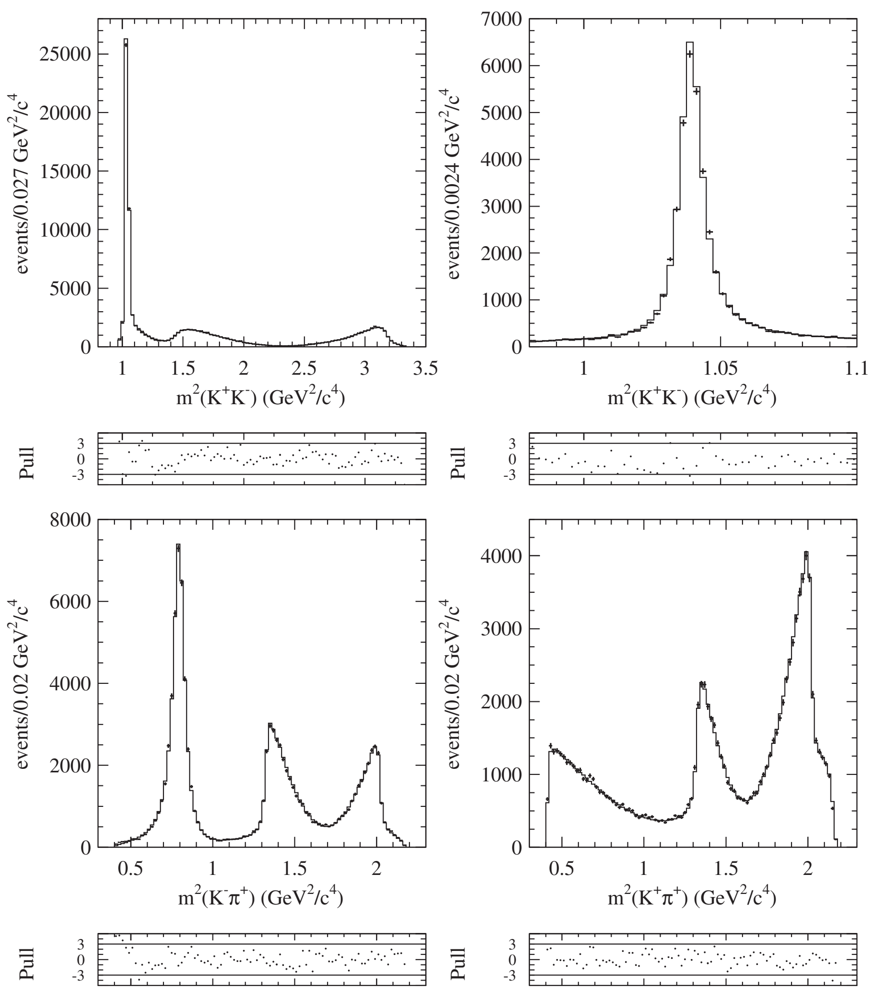

FIG. 9. $D_s^+ \to K^+K^-\pi^+$: Dalitz plot projections from the best fit. The data are represented by points with error bars, the fit results by the histograms.

Another way to test the fit quality is to project the fit results onto the $\langle Y_k^0\rangle$ moments, shown in Fig. 10 for the K^+K^- system and Fig. 11 for the $K^-\pi^+$ system. We observe that the fit results reproduce the data projections for moments up to $k = 7$, indicating that the fit describes the details of the Dalitz plot structure very well. The $K^-\pi^+$ $\langle Y_3^0\rangle$ and $\langle Y_5^0\rangle$ moments show activity in the $\bar{K}^*(892)^0$ region which the Dalitz plot analysis relates to interference between the $\bar{K}^*(892)^0K^+$ and $f_0(1710)\pi^+$ decay amplitudes. This seems to be a reasonable explanation for the failure of the model-independent $K^-\pi^+$ analysis (Sec. V C), although the fit still does not provide a good description of the $\langle Y_3^0\rangle$ and $\langle Y_5^0\rangle$ moments in this mass region.

We check the consistency of the Dalitz plot results and those of the analysis described in Sec. V B. We compute the amplitude and phase of the $f_0(980)/\mathcal{S}$ wave relative to the $\phi(1020)/\mathcal{P}$ wave and find good agreement.

A. Systematic errors

Systematic errors given in Table V and in other quoted results take into account:

(i) Variation of the R_r and $R_{D_s^+}$ constants in the Blatt-Weisskopf penetration factors within the range [0–3] GeV^{-1} and [1–5] GeV^{-1}, respectively.

(ii) Variation of fixed resonance masses and widths within the $\pm1\sigma$ error range quoted in Ref. [10].

(iii) Variation of the efficiency parameters within $\pm1\sigma$ uncertainty.

(iv) Variation of the purity parameters within $\pm1\sigma$ uncertainty.

(v) Fits performed with the use of the lower/upper sideband only to parametrize the background.

(vi) Results from fits with alternative sets of signal amplitude contributions that give equivalent Dalitz plot descriptions and similar sums of fractions.

(vii) Fits performed on a sample of 100 000 events selected by applying a looser likelihood-ratio criterion but selecting a narrower ($\pm 1\sigma_{D_s^+}$) signal region. For this sample the purity is roughly the same as for the nominal sample ($\simeq 94.9\%$).

B. Comparison between Dalitz plot analyses of $D_s^+ \to K^+K^-\pi^+$

Table VII shows a comparison of the Dalitz plot fit fractions, shown in Table V, with the results of the analyses performed by the E687 [8] and CLEO [9] Collaborations. The E687 model is improved by adding a $f_0(1370)$ amplitude and leaving the $\bar{K}^*(892)^0$ parameters free in the fit.

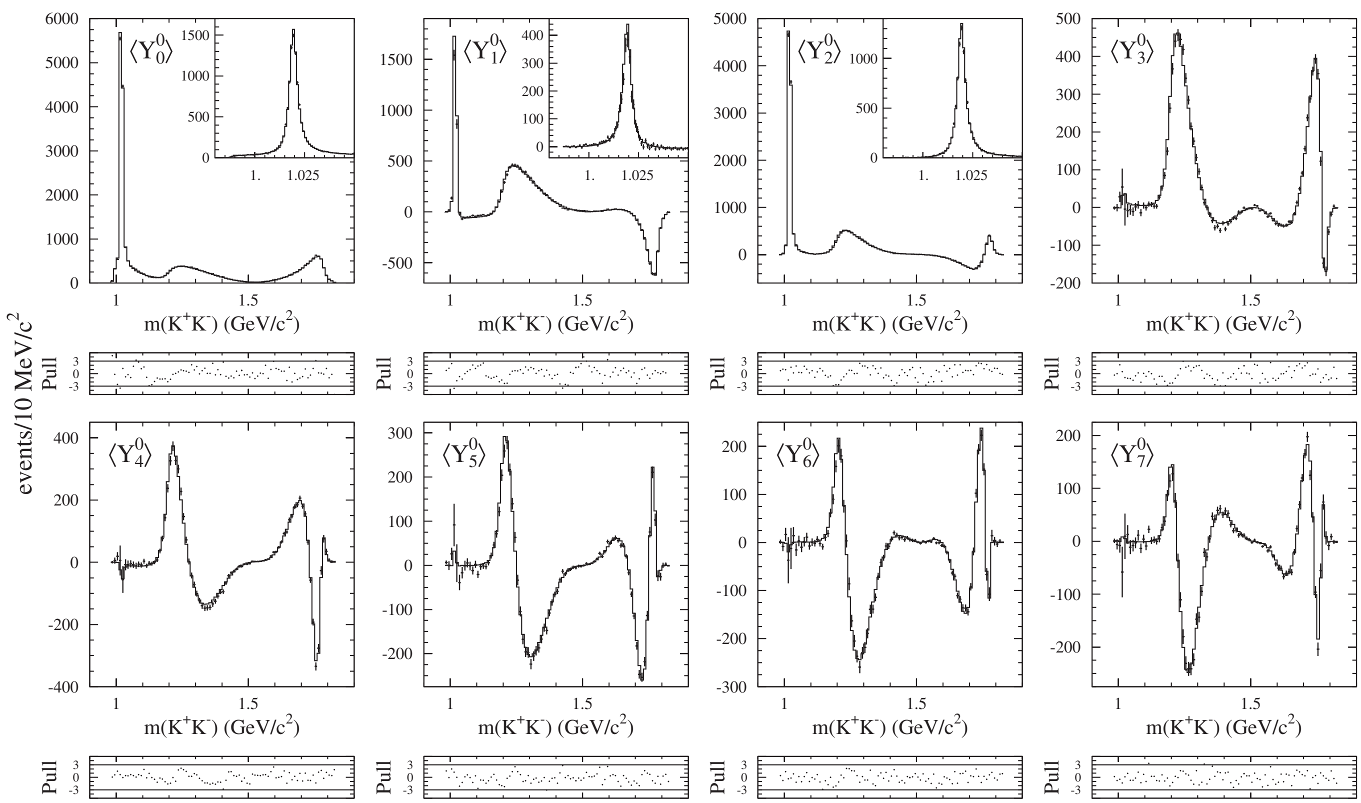

FIG. 10. K^+K^- mass dependence of the spherical harmonic moments, $\langle Y_k^0\rangle$, obtained from the fit to the $D_s^+ \to K^+K^-\pi^+$ Dalitz plot compared to the data moments. The data are represented by points with error bars, the fit results by the histograms. The insets show an expanded view of the $\phi(1020)$ region.

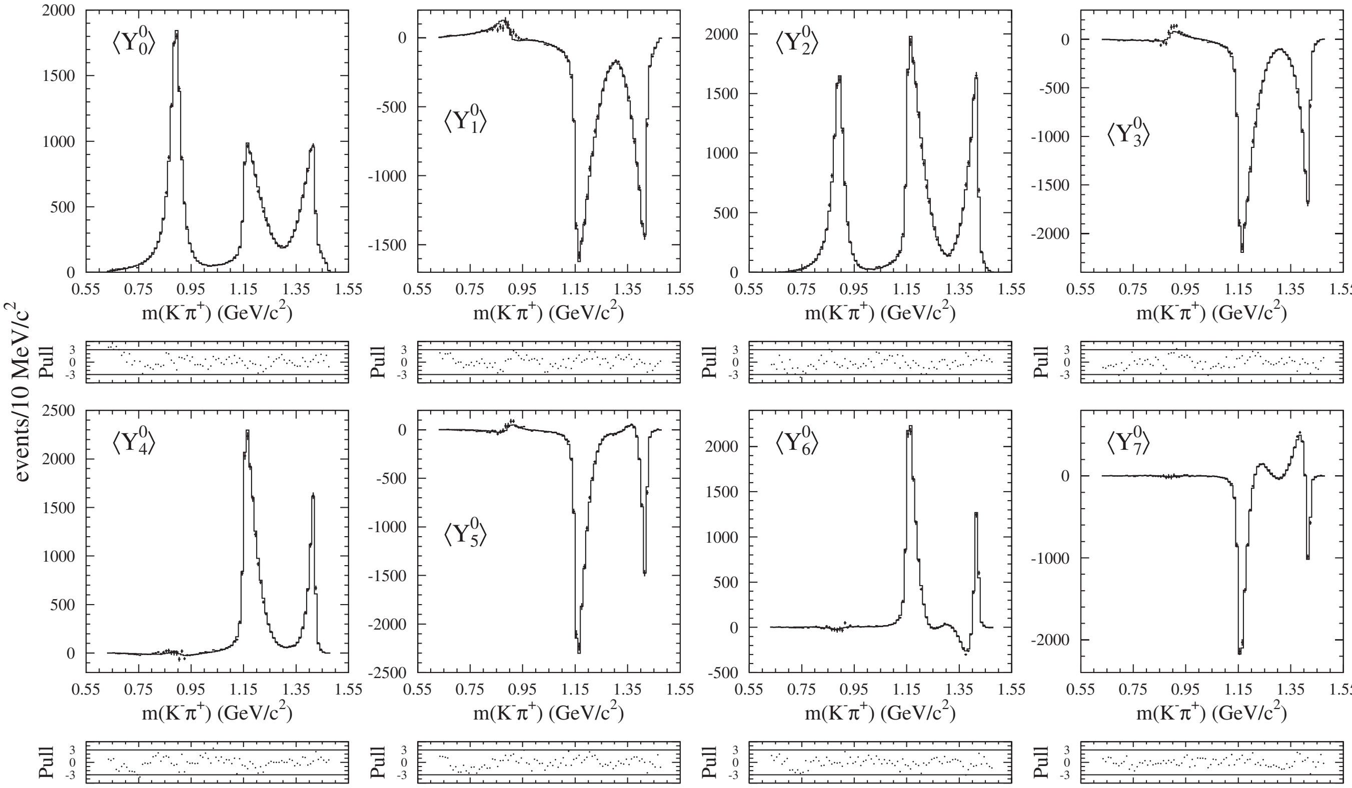

FIG. 11. $K^-\pi^+$ mass dependence of the spherical harmonic moments, $\langle Y_k^0\rangle$, obtained from the fit to the $D_s^+ \to K^+K^-\pi^+$ Dalitz plot compared to the data moments. The data are represented by points with error bars, the fit results by the histograms.

We find that the $\bar{K}^*(892)^0$ width [Eq. (30)] is about 3 MeV lower than that in Ref. [10]. This result is consistent with the width measured by CLEO-c Collaboration ($\Gamma_{\bar{K}^*(892)^0} = 45.7 \pm 1.1$ MeV).

What is new in this analysis is the parametrization of the K^+K^- $\mathcal{S}$ wave at the K^+K^- threshold. While E687 and CLEO-c used a coupled channel BW (Flatté) amplitude [17] to parametrize the $f_0(980)$ resonance, we use the model-independent parametrization described in Sec. V B. This approach overcomes the uncertainties that affect the coupling constants $g_{\pi\pi}$ and g_{KK} of the $f_0(980)$, and any argument about the presence of an $a(980)$ meson decaying to K^+K^-. The model, described in this paper, returns a more accurate description of the event distribution on the Dalitz plot ($\chi^2/\nu = 1.2$) and smaller $f_0(980)$ and total fit fractions with respect to the CLEO-c result. In addition the goodness of fit in this analysis is tested by an adaptive binning χ^2, a tool more suitable when most of the events are gathered in a limited region of the Dalitz plot.

Finally, we observe that the phase of the $\phi(1020)$ amplitude ($166° \pm 1° \pm 2°$) is consistent with the E687 result ($178° \pm 20° \pm 24°$) but is roughly shifted by 180° respect to the CLEO-c result ($-8° \pm 4° \pm 4°$).

TABLE VII. Comparison of the fitted decay fractions with the Dalitz plot analyses performed by E687 and CLEO-c Collaborations.

	Decay fraction (%)		
Decay mode	*BABAR*	E687	CLEO-c
$\bar{K}^*(892)^0K^+$	$47.9 \pm 0.5 \pm 0.5$	$47.8 \pm 4.6 \pm 4.0$	$47.4 \pm 1.5 \pm 0.4$
$\phi(1020)\pi^+$	$41.4 \pm 0.8 \pm 0.5$	$39.6 \pm 3.3 \pm 4.7$	$42.2 \pm 1.6 \pm 0.3$
$f_0(980)\pi^+$	$16.4 \pm 0.7 \pm 2.0$	$11.0 \pm 3.5 \pm 2.6$	$28.2 \pm 1.9 \pm 1.8$
$\bar{K}_0^*(1430)^0K^+$	$2.4 \pm 0.3 \pm 1.0$	$9.3 \pm 3.2 \pm 3.2$	$3.9 \pm 0.5 \pm 0.5$
$f_0(1710)\pi^+$	$1.1 \pm 0.1 \pm 0.1$	$3.4 \pm 2.3 \pm 3.5$	$3.4 \pm 0.5 \pm 0.3$
$f_0(1370)\pi^+$	$1.1 \pm 0.1 \pm 0.2$	⋯	$4.3 \pm 0.6 \pm 0.5$
Sum	$110.2 \pm 0.6 \pm 2.0$	111.1	$129.5 \pm 4.4 \pm 2.0$
χ^2/NDF	$\frac{2843}{(2305-14)} = 1.2$	$\frac{50.2}{33} = 1.5$	$\frac{178}{117} = 1.5$
Events	96307 ± 369	701 ± 36	12226 ± 22

VIII. SINGLY-CABIBBO-SUPPRESSED $D_s^+ \to K^+K^-K^+$, AND DOUBLY-CABIBBO-SUPPRESSED $D_s^+ \to K^+K^-\pi^-$ DECAY

In this section we measure the branching ratio of the SCS decay channel (2) and of the DCS decay channel (3) with respect to the CF decay channel (1). The two channels are reconstructed using the method described in Sec. III with some differences related to the particle-identification of the D_s^+ daughters. For channel (2) we require the identification of three charged kaons while for channel (3) we require the identification of one pion and two kaons having the same charge. We use both the D_s^{*+} identification and the likelihood ratio to enhance the signal with respect to background as described in Sec. III.

The ratios of branching fractions are computed as

$$\frac{\mathcal{B}(D_s^+ \to K^+K^-K^+)}{\mathcal{B}(D_s^+ \to K^+K^-\pi^+)} = \frac{N_{D_s^+\to K^+K^-K^+}}{N_{D_s^+\to K^+K^-\pi^+}} \times \frac{\epsilon_{D_s^+\to K^+K^-\pi^+}}{\epsilon_{D_s^+\to K^+K^-K^+}} \tag{32}$$

and

$$\frac{\mathcal{B}(D_s^+ \to K^+K^+\pi^-)}{\mathcal{B}(D_s^+ \to K^+K^-\pi^+)} = \frac{N_{D_s^+\to K^+K^+\pi^-}}{N_{D_s^+\to K^+K^-\pi^+}} \times \frac{\epsilon_{D_s^+\to K^+K^-\pi^+}}{\epsilon_{D_s^+\to K^+K^+\pi^-}}. \tag{33}$$

Here the N values represent the number of signal events for each channel, and the ϵ values indicate the corresponding detection efficiencies.

To compute these efficiencies, we generate signal MC samples having uniform distributions across the Dalitz plots. These MC events are reconstructed as for data events, and the same particle-identification criteria are applied. Each track is weighted by the data-MC discrepancy in particle-identification efficiency obtained independently from high statistics control samples. A systematic uncertainty is assigned to the use of this weight. The generated and reconstructed Dalitz plots are divided into 50×50 cells and the Dalitz plot efficiency is obtained as the ratio of reconstructed to generated content of each cell. In this way the efficiency for each event depends on its location on the Dalitz plot. By varying the likelihood-ratio criterion, the sensitivity S of $D_s^+ \to K^+K^-K^+$ is maximized. The sensitivity is defined as $S = N_s/\sqrt{N_s + N_b}$, where s and b indicate signal and background. To reduce systematic uncertainties, we then apply the same likelihood-ratio criterion to the $D_s^+ \to K^+K^-\pi^+$ decay. We then repeat this procedure to find an independently optimized selection criterion for the $D_s^+ \to K^+K^+\pi^-$ to $D_s^+ \to K^+K^-\pi^+$ ratio.

The branching ratio measurements are validated using a fully inclusive $e^+e^- \to c\bar{c}$ MC simulation incorporating all known charmed meson decay modes. The MC events are subjected to the same reconstruction, event selection, and analysis procedures as for the data. The results are found to be consistent, within statistical uncertainty, with the branching fraction values used in the MC generation.

A. Study of $D_s^+ \to K^+K^-K^+$

The resulting $K^+K^-K^+$ mass spectrum is shown in Fig. 12(a). The D_s^+ yield is obtained by fitting the mass spectrum using a Gaussian function for the signal, and a linear function for the background. The resulting yield is reported in Table I.

The systematic uncertainties are summarized in Table VIII and are evaluated as follows:

(i) The effect of MC statistics is evaluated by randomizing each efficiency cell on the Dalitz plot according to its statistical uncertainty.

(ii) The selection made on the D_s^{*+} candidate Δm is varied to $\pm 2.5\sigma_{D_s^{*+}}$ and $\pm 1.5\sigma_{D_s^{*+}}$.

(iii) For particle identification we make use of high statistics control samples to assign 1% uncertainty to each kaon and 0.5% to each pion.

(iv) The effect of the likelihood-ratio criterion is studied by measuring the branching ratio for different choices.

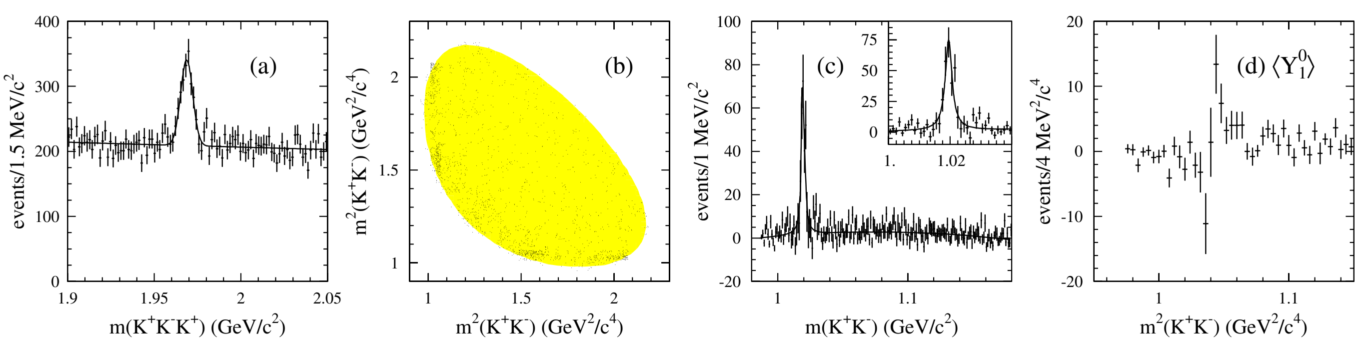

FIG. 12 (color online). (a) $K^+K^-K^+$ mass spectrum showing a D_s^+ signal. The curve is the result of the fit described in the text. (b) Symmetrized Dalitz plot, (c) K^+K^- mass spectrum (two combinations per event), and (d) the $\langle Y_1^0 \rangle$ moment. The insert in (c) shows an expanded view of the $\phi(1020)$ region. The Dalitz plot and its projection are background subtracted and efficiency corrected. The curve results from the fit described in the text.

TABLE VIII. Summary of systematic uncertainties on the measurement of the $D_s^+ \to K^+K^-K^+$ branching ratio.

Uncertainty	$\frac{\mathcal{B}(D_s^+\to K^+K^-K^+)}{\mathcal{B}(D_s^+\to K^+K^-\pi^+)}$
MC statistics	2.6%
Δm	0.3%
Likelihood-ratio	3.5%
PID	1.5%
Total	4.6%

We measure the following branching ratio:

$$\frac{\mathcal{B}(D_s^+ \to K^+K^-K^+)}{\mathcal{B}(D_s^+ \to K^+K^-\pi^+)} = (4.0 \pm 0.3_{\rm stat} \pm 0.2_{\rm syst}) \times 10^{-3}. \tag{34}$$

A Dalitz plot analysis in the presence of a high level of background is difficult, therefore we can only extract empirically some information on the decay. Since there are two identical kaons into the final state, the Dalitz plot is symmetrized by plotting two combinations per event ($[m^2(K^-K_1^+), m^2(K^-K_2^+)]$ and $[m^2(K^-K_2^+), m^2(K^-K_1^+)]$). The symmetrized Dalitz plot in the $D_s^+ \to K^+K^-K^+$ signal region, corrected for efficiency and background subtracted, is shown in Fig. 12(b). It shows two bands due to the $\phi(1020)$ and no other structure, indicating a large contribution via $D_s^+ \to \phi(1020)K^+$. To test the possible presence of $f_0(980)$, we plot, in Fig. 12(d), the distribution of the $\langle Y_1^0 \rangle$ moment; θ is the angle between the K^+ direction in the K^+K^- rest frame and the prior direction of the K^+K^- system in the D_s^+ rest frame. We observe the mass dependence characteristic of interference between $\mathcal{S}$- and $\mathcal{P}$-wave amplitudes, and conclude that there is a contribution from $D_s^+ \to f_0(980)K^+$ decay, although its branching fraction cannot be determined in the present analysis.

An estimate of the $\phi(1020)K^+$ fraction can be obtained from a fit to the K^+K^- mass distribution [Fig. 12(c)]. The mass spectrum is fitted using a relativistic BW for the $\phi(1020)$ signal, and a second order polynomial for the background. We obtain:

$$\frac{\mathcal{B}(D_s^+ \to \phi K^+) \cdot \mathcal{B}(\phi \to K^+K^-)}{\mathcal{B}(D_s^+ \to K^+K^-K^+)} = 0.41 \pm 0.08_{\rm stat} \pm 0.03_{\rm syst}. \tag{35}$$

The systematic uncertainty includes the contribution due to Δm and the likelihood-ratio criteria, the fit model, and the background parametrization.

B. Study of $D_s^+ \to K^+K^+\pi^-$

Figure 13(a) shows the $K^+K^+\pi^-$ mass spectrum. A fit with a Gaussian signal function and a linear background function gives the yield presented in Table I. To minimize systematic uncertainty, we apply the same likelihood-ratio criteria to the $K^+K^+\pi^-$ and $K^+K^-\pi^+$ final states, and correct for the efficiency evaluated on the Dalitz plot. The branching ratio which results is

$$\frac{\mathcal{B}(D_s^+ \to K^+K^+\pi^-)}{\mathcal{B}(D_s^+ \to K^+K^-\pi^+)} = (2.3 \pm 0.3_{\rm stat} \pm 0.2_{\rm syst}) \times 10^{-3}. \tag{36}$$

This value is in good agreement with the Belle measurement: $\frac{\mathcal{B}(D_s^+\to K^+K^+\pi^-)}{\mathcal{B}(D_s^+\to K^+K^-\pi^+)} = (2.29 \pm 0.28 \pm 0.12) \times 10^{-3}$ [11].

Table IX lists the results of the systematic studies performed for this measurement; these are similar to those used in Sec. VIII A. The particle-identification systematic is not taken in account because the final states differ only in the charge assignments of the daughter tracks.

The symmetrized Dalitz plot for the signal region, corrected for efficiency and background subtracted, is shown in Fig. 13(b). We observe the presence of a significant

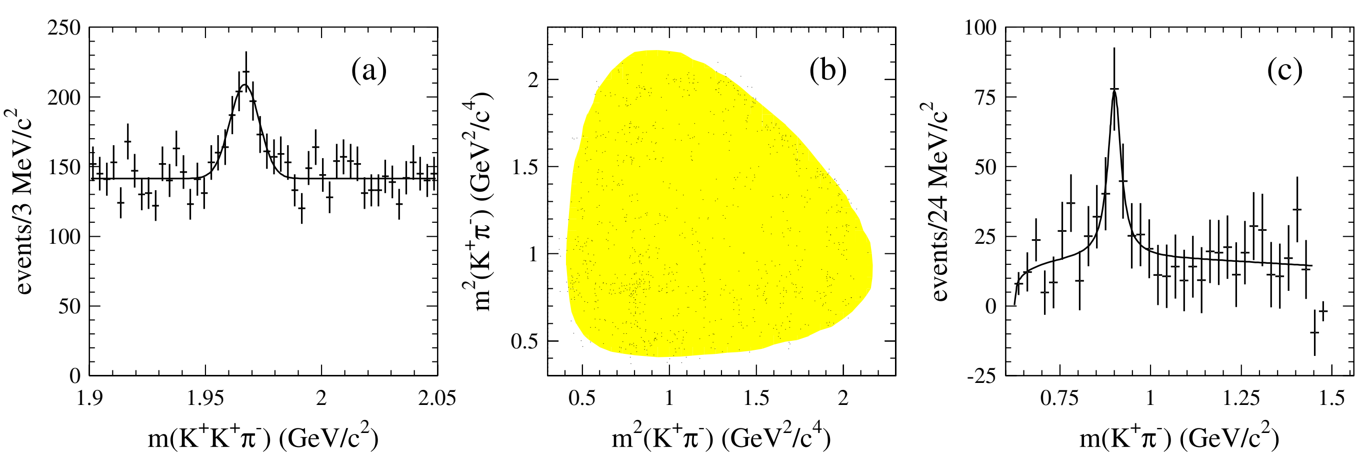

FIG. 13 (color online). (a) $K^+K^+\pi^-$ mass spectrum showing a D_s^+ signal. (b) Symmetrized Dalitz plot for $D_s^+ \to K^+K^+\pi^-$ decay. (c) $K^+\pi^-$ mass distribution (two combinations per event). The Dalitz plot and its projection are background subtracted and efficiency corrected. The curves result from the fits described in the text.

TABLE IX. Summary of systematic uncertainties in the measurement of the $D_s^+ \to K^+K^+\pi^-$ relative branching fraction.

Uncertainty	$\frac{\mathcal{B}(D_s^+ \to K^+K^+\pi^-)}{\mathcal{B}(D_s^+ \to K^+K^-\pi^+)}$
MC statistics	0.04%
Δm	4.7%
Likelihood-ratio	6.0%
Total	7.7%

$K^*(892)^0$ signal, which is more evident in the $K^+\pi^-$ mass distribution, shown in Fig. 13(c). Fitting this distribution using a relativistic $\mathcal{P}$-wave BW signal function and a threshold function, we obtain the following fraction for this contribution:

$$\frac{\mathcal{B}(D_s^+ \to K^*(892)^0 K^+) \cdot \mathcal{B}(K^*(892)^0 \to K^+\pi^-)}{\mathcal{B}(D_s^+ \to K^+K^+\pi^-)} = 0.47 \pm 0.22_{\mathrm{stat}} \pm 0.15_{\mathrm{syst}}. \quad (37)$$

Systematic uncertainty contributions include those from Δm and the likelihood-ratio criteria, the fitting model, and the background parametrization.

The symmetrized Dalitz plot shows also an excess of events at low K^+K^+ mass, which may be due to a Bose-Einstein correlation effect [26]. We remark, however, that this effect is not visible in $D_s^+ \to K^+K^-K^+$ decay [Fig. 12(b)].

IX. CONCLUSIONS

In this paper we perform a high statistics Dalitz plot analysis of $D_s^+ \to K^+K^-\pi^+$, and extract amplitudes and phases for each resonance contributing to this decay mode. We also make a new measurement of the $\mathcal{P}$-wave/$\mathcal{S}$-wave ratio in the $\phi(1020)$ region. The K^+K^- $\mathcal{S}$ wave is extracted in a quasi–model-independent way, and complements the $\pi^+\pi^-$ $\mathcal{S}$ wave measured by this experiment in a previous publication [4]. Both measurements can be used to obtain new information on the properties of the $f_0(980)$ state [27]. We also measure the relative and partial branching fractions for the SCS $D_s^+ \to K^+K^-K^+$ and DCS $D_s^+ \to K^+K^+\pi^-$ decays with high precision.

ACKNOWLEDGMENTS

We are grateful for the extraordinary contributions of our PEP-II colleagues in achieving the excellent luminosity and machine conditions that have made this work possible. The success of this project also relies critically on the expertise and dedication of the computing organizations that support *BABAR*. The collaborating institutions wish to thank SLAC for its support and the kind hospitality extended to them. This work is supported by the US Department of Energy and National Science Foundation, the Natural Sciences and Engineering Research Council (Canada), the Commissariat à l'Energie Atomique and Institut National de Physique Nucléaire et de Physique des Particules (France), the Bundesministerium für Bildung und Forschung and Deutsche Forschungsgemeinschaft (Germany), the Istituto Nazionale di Fisica Nucleare (Italy), the Foundation for Fundamental Research on Matter (The Netherlands), the Research Council of Norway, the Ministry of Education and Science of the Russian Federation, Ministerio de Ciencia e Innovación (Spain), and the Science and Technology Facilities Council (United Kingdom). Individuals have received support from the Marie-Curie IEF program (European Union), the A. P. Sloan Foundation (USA), and the Binational Science Foundation (USA-Israel).

[1] E. M. Aitala *et al.* (E791 Collaboration), Phys. Rev. Lett. **89**, 121801 (2002); M. Ablikim *et al.* (BES Collaboration), Phys. Lett. B **633**, 681 (2006).

[2] E. M. Aitala *et al.* (E791 Collaboration), Phys. Rev. Lett. **86**, 765 (2001); M. Ablikim *et al.* (BES Collaboration), Phys. Lett. B **598**, 149 (2004).

[3] See for example F. E. Close and N. A. Tornqvist, J. Phys. G **28**, R249 (2002).

[4] B. Aubert *et al.* (*BABAR* Collaboration), Phys. Rev. D **79**, 032003 (2009).

[5] S. Stone and L. Zhang, Phys. Rev. D **79**, 074024 (2009).

[6] Y. Xie, P. Clarke, G. Cowan, and F. Muheim, J. High Energy Phys. 09 (2009) 074.

[7] All references in this paper to an explicit decay mode imply the use of the charge conjugate decay also.

[8] P. L. Frabetti *et al.* (E687 Collaboration), Phys. Lett. B **351**, 591 (1995).

[9] R. E. Mitchell *et al.* (CLEO Collaboration), Phys. Rev. D **79**, 072008 (2009).

[10] K. Nakamura *et al.* (Particle Data Group), J. Phys. G **37**, 075021 (2010).

[11] B. R. Ko *et al.* (Belle Collaboration), Phys. Rev. Lett. **102**, 221802 (2009).

[12] B. Aubert *et al.* (*BABAR* Collaboration), Nucl. Instrum. Methods Phys. Res., Sect. A **479**, 1 (2002).

[13] B. Aubert *et al.* (*BABAR* Collaboration), Phys. Rev. D **65**, 091104(R) (2002).

[14] S. Agostinelli *et al.* (GEANT4 Collaboration), Nucl. Instrum. Methods Phys. Res., Sect. A **506**, 250 (2003).

[15] S. U. Chung, Phys. Rev. D **56**, 7299 (1997).

[16] B. Aubert *et al.* (*BABAR* Collaboration), Phys. Rev. D **78**, 051101(R) (2008).
[17] S. M. Flatté *et al.*, Phys. Lett. **38B**, 232 (1972).
[18] B. Aubert *et al.* (*BABAR* Collaboration), Phys. Rev. D **72**, 052008 (2005).
[19] B. Aubert *et al.* (*BABAR* Collaboration), Phys. Rev. D **76**, 011102(R) (2007).
[20] L. Maiani, A. D. Polosa, and V. Riquer, Phys. Lett. B **651**, 129 (2007).
[21] K. S. Kölbig, CERN Program Library, Report No. D110.
[22] D. Asner, arXiv:hep-ex/0410014; S. Eidelman *et al.* (Particle Data Group), Phys. Lett. B **592**, 495 (2004).
[23] J. M. Blatt and V. F. Weisskopf, *Theoretical Nuclear Physics* (John Wiley and Sons, New York, 1952).
[24] D. Aston *et al.* (LASS Collaboration), Nucl. Phys. **B296**, 493 (1988).
[25] P. del Amo Sanchez *et al.* (*BABAR* Collaboration), Phys. Rev. Lett. **105**, 081803 (2010).
[26] G. Goldhaber, S. Goldhaber, W. Y. Lee, and A. Pais, Phys. Rev. **120**, 300 (1960).
[27] M. R. Pennington, in *Proceedings of 11th International Conference on Meson-Nucleon Physics and the Structure of the Nucleon (MENU 2007), Julich, Germany* econf C070910: 106 (2007), p. 106.